

- CIPS cloud wind tracking algorithm is elaborated and the wind product is assessed.
- Multiple searching frame sizes are adopted to create robust winds.
- Preliminary wind sets are then merged and edited to obtain final product.
- CIPS zonal and meridional winds conform to climatology.
- Meridional wind intraseasonal variation pattern is susceptible to the sampling path.

# AIM CIPS PMC tracking wind product retrieval approach and first assessment

P. P. Rong<sup>1</sup>, J. Yue<sup>1</sup>, J. M. Russell III<sup>1</sup>, J. D. Lumpe<sup>2</sup>, D. E. Siskind<sup>3</sup>, and C. E. Randall<sup>4</sup>

1. Center for Atmospheric Sciences, Hampton University, Hampton, Virginia, USA

2. Computational Physics, Inc., Boulder, Colorado, USA

3. Naval Research Lab, Washington DC, USA

4. Laboratory for Atmospheric and Space Physics, University of Colorado Boulder, USA

\*Corresponding author email: ping-ping.rong@hamptonu.edu

Mailing address: 23 E. Tyler street, Hampton, VA23668

1 **Abstract:**

2 The refined Cloud Imaging and Particle-Size (CIPS) cloud wind tracking algorithm is elaborated and  
3 the wind product is assessed against the Navy Operational Global Atmospheric Prediction System -  
4 Advanced Level Physics and High Altitude (NOGAPS-ALPHA) winds and the horizontal wind model  
5 (HWM14) climatological winds. Multiple searching frame sizes are adopted to generate the preliminary  
6 wind sets which are then merged and further edited based on the clustering of the similar wind directions  
7 ( $\pm 20^\circ$ ). The mean values of the clusters within the sampling grids of  $1.5^\circ \times 1.5^\circ$  or  $4.5^\circ \times 4.5^\circ$  are taken as the  
8 final wind product. At the coincidences the CIPS and NOGAPS winds show a moderate degree of  
9 deterministic consistency. We have further shown that on the orbit-to-orbit basis when the NOGAPS  
10 modeled ice and CIPS measured ice correlate better, the wind agreement is also better. The difference in  
11 the two wind sets is most likely attributed to NOGAPS temperature being deviated from the true  
12 temperature that will affect the geostrophic component of the winds and also to the fact that the CIPS winds  
13 are often ageostrophic and are cascaded into smaller scales. The CIPS zonal (westward) winds are  
14 decreased and then reversed in early June and late August whereas in the core of the season they are  
15 stronger. This overall variation pattern is shared by both NOGAPS and HWM14 zonal winds. Both  
16 NOGAPS and HWM14 zonal winds exhibit ~8-10 m/s difference between cases using all local times (LTs)  
17 and the CIPS LT range of 13-22 hour due to the dominant diurnal migrating tides, and this may partially  
18 interpret the weaker CIPS zonal winds. The meridional (equatorward) winds do not follow any established  
19 intra-seasonal variation pattern but rather the variability is susceptible to the sampling longitudes/latitudes.  
20  
21  
22  
23  
24  
25  
26  
27  
28  
29  
30  
31  
32  
33  
34

35 **Keywords:** cloud wind tracking, CIPS PMCs, pattern matching algorithm, wind assessment  
36  
37  
38  
39  
40  
41  
42  
43  
44  
45  
46  
47  
48  
49  
50  
51  
52  
53  
54  
55  
56  
57  
58  
59  
60  
61  
62  
63  
64  
65

## 1. Introduction

The cloud motion vectors (CMVs) are derived by a three-step procedure. The initial step selects target, the second step assigns altitude, and the third step derives motion. Motion is derived by a pattern recognition algorithm that matches the feature within the targeted area in one image within the search area [Menzel, 2001]. Traditional cloud wind tracking is often carried out in the troposphere where the cloud coverage is the largest and the occurrence most frequent.

Polar mesospheric clouds (PMCs), or noctilucent clouds (NLCs) [e.g., Foerster and Jesse, 1892; Fogle and Haurwitz, 1966] are thin water ice clouds that are regularly observed poleward of 60°N/S at approximately an altitude of ~83 km which is the highest place in the Earth atmosphere water ice clouds could ever exist. The PMC formation is attributed to the low temperature and enhanced H<sub>2</sub>O abundance driven by the upward transport branch of the residual meridional circulation in the polar summer region [Garcia, 1989]. The wind measurements for this altitude and latitude range are rare and are mostly from the ground-based measurements [e.g., Portnyagin et al., 2004a; Hoffmann et al., 2011; Latteck et al., 2012; Renkwitz et al., 2018], and a small number of satellite measurements taken by the UARS High Resolution Doppler Imager (HRDI, 50-115 km, 1993-1994) and Wind Imaging Interferometer (WINDII, 90-120 km, 1991-1996) [e.g., Drob et al., 2008; 2015]. Employing PMCs or NLCs as wind tracers began as early as 1892 by Foerster and Jesse, and other successors also have carried out similar studies such as by Baumgarten et al., [2002] and Dalin et al. [2013]. Berger and von Zahn [2007] used a Lagrangian model to show that ice observed at 69°N could be nucleated 9° poleward and the averaged transport time could be as long as 36 hours. Given the originality of these studies, the PMC/NLC wind tracking operation was only carried out within limited spatial region and time periods. In addition, even if they are available, the poor availability of the correlative wind sets would pose difficulty to the validation of the wind tracking results.

Cloud or moisture tracking is an established approach that is widely applied in deriving the tropospheric winds. In a recent study by Mueller et al. [2017] the CMV product retrieved from the Multi-angle Imaging SpectroRadiometer (MISR) instrument on the polar-orbiting Terra satellite is assessed through coincidence analysis with several contemporary data sets of the atmospheric motion vectors (AMVs). The Terra satellite swath width is of 360 km, and the height-assigned CMVs are obtained from a single overpass by tracking feature progression within MISR red-band imagery over the 3.5-min interval between the initial 70° forward view and the nadir (0°) view and then again for the same interval between the nadir view and the final 70° aft view [Horváth and Davies 2001; Mueller et al. 2013]. Due to the small time interval and a large view angle difference, a 0.5 km cloud height error (for example) can cause ~6.7 m/s of wind error along-track, which is notably large, due to the stereoscopic parallax. Also given the fact that the tropospheric cloud height varies in an extended range of 2 km – 16 km, stereoscopic parallax can

1 be a significant error source to the MISR CMVs. Features are tracked by a pattern matching algorithm  
2 applied to different resampling resolutions, i.e., 1.1 km, 0.55 km, and 0.275 km, to obtain robust matching  
3 results, with roughly consistent frame sizes of 6-8 km. Assuming a tropospheric jet speed of 32 m/s [Wu et  
4 al., 2015], after 3.5 minutes the cloud pattern movement is about 6.7 km which is close to the frame size  
5 and meanwhile this distance far exceeds the pixel size (i.e., 0.275 km), i.e., by ~25 times. The underlying  
6 mechanism of the MISR cloud height and motion retrievals consists of two steps, correspondence and  
7 reconstruction. That is, (1) identifying conjugates, the apparent image coordinates as captured (at different  
8 times for the same cloud feature) by two or more of MISR's nine cameras during an overpass at a given  
9 surface ellipsoid, and (2) subsequently inferring the true position (including the cloud height) and  
10 horizontal motion of each such feature by intersecting known camera lines of sight associated with  
11 conjugate image coordinates. In summary, in the first step a successful pattern matching is being achieved;  
12 and in the second step, reconstruction infers the position, i.e., both horizontal and height, of the feature  
13 associated with that conjugate.  
14  
15  
16  
17  
18  
19  
20  
21  
22  
23

24 The fact that PMCs are a layered phenomenon, i.e., with a centroid height at ~83 km, enables the  
25 longitude/latitude (lon/lat hereinafter) registration more definitive than the tropospheric clouds. Russell et  
26 al. [2011] indicated that the PMC height variability could reach ~3 km throughout the season and for  
27 different hemispheres, with the southern hemispheric PMC being systematically higher. Under such an  
28 estimate the parallax still exists when the camera view angle is deviated from zero. In the current paper the  
29 AIM Cloud Imaging and Particle Size (CIPS) experiment [McClintock et al., 2009] PMC wind tracking is  
30 documented. In the CIPS retrieval a constant cloud deck height of 83 km is assumed [Lumpe et al., 2013]  
31 and the lons and lats are registered prior to the cloud tracking operation. The CIPS instrument is able to  
32 achieve a global coverage within a day by providing 14-15 "push-broom" orbital strips with a cross-track  
33 width of about 800 km which is about twice as wide as MISR swath. The CIPS cloud coverage achieves  
34 strong overlaps north/south of 70°N/S between orbits. This would allow all directions of wind detections so  
35 that the wind tracking results are less biased which might stem from the east-to-west orbital progress. A  
36 feasibility study on the CIPS cloud wind tracking was carried out by Rong et al. [2015] via exploring the  
37 results both on the same orbit and between two adjacent orbits using two test periods of five days each in  
38 July and August 2007 respectively. In the along-track direction stacks of highly overlapped images occur  
39 and there are a total of 27 images along one orbit. The nadir and the front or aft view cameras have a view  
40 angle difference of maximally 60° which is similar to MISR. The spatial footprints of the four CIPS  
41 cameras, especially the forward and aft cameras, result in one bowtie shaped image assuming a constant  
42 cloud deck of 83 km as mentioned above. As the PMC height fluctuates within  $\sim\pm 3$  km it will cause  
43 uncertainty in the lon and lat registration. In CIPS level-2 data production images from all cameras are used  
44  
45  
46  
47  
48  
49  
50  
51  
52  
53  
54  
55  
56  
57  
58  
59  
60  
61  
62  
63  
64  
65

1 to determine the lons and lats prior to the wind tracking and therefore a simultaneous retrieval of the  
2 lon/lat/height is not required. For example, the worst horizontal displacement error for a 3 km height  
3 difference is about 5 km (i.e., about one CIPS pixel size) assuming the maximum of 60° view angle, and  
4 the corresponding velocity difference is close to 1.0 m/s given 96 minutes of time interval which is small  
5 compared to the mean zonal wind speed of ~20 m/s in the PMC region.  
6  
7  
8

9  
10 The CIPS cloud tracking was initially applied to both the one-orbit across and 7-scenes across (for the  
11 same orbit) cases [Rong et al., 2015]. In the 7-scenes across scenario, the time interval of the progressive  
12 images is roughly 3-4 minutes, which is a similar to that in the MISR cloud tracking. However, the CIPS  
13 horizontal resolution varies in the range of 2-7 km which is 7-25 times coarser than MISR. Within 3-4  
14 minutes a 20 m/s wind speed would lead to a merely 4-5 km of movement which is comparable to the  
15 image horizontal resolution. After the actual matching test using two 5-days periods as shown in the Fig. 11  
16 in Rong et al. [2015] we found that ~80-90% of the matches are only displaced by 0-2 pixels. Even a wind  
17 speed of 100 m/s, which is considered unusually large in the PMC region, only leads to 4-5 pixels of  
18 displacement in the same CIPS orbit. These displacements are too small to derive reliable wind speeds.  
19 Therefore, scenes from the same CIPS orbit are not sufficient to derive accurate winds.  
20  
21  
22  
23  
24  
25  
26  
27

28  
29 The consecutive two orbits with longer time interval (i.e., 96 minutes) are eventually adopted for the  
30 CIPS wind tracking but the PMC patterns will likely experience considerable variation over this time  
31 mainly due to the change in the environmental temperature or H<sub>2</sub>O. In some cases the rapid change of  
32 temperature and H<sub>2</sub>O could simply deform the pattern to the point that it is no longer recognizable,  
33 resulting in failed match. But in many cases the pattern remains identifiable although there could be a  
34 systematic change in brightness, which may reflect the impact from the larger scale waves. This latter case  
35 will be discussed in a following section through examining actual examples of matches.  
36  
37  
38  
39  
40  
41

42 Algorithm refining and the quality control of the derived winds are vital steps of the cloud tracking  
43 operation [e.g., Menzel, 2001], which has been extensively applied in the MISR tropospheric wind tracking  
44 described in Muller et al. [2017; 2013]. Accurately reconstructing motion vectors consisting of height and  
45 both axes of horizontal motion requires input conjugates specifying coordinates for three cameras (i.e.,  
46 conjugate triplets) spanning a large view angle difference. A clustering algorithm is used to independently  
47 derive forward and aft 17.6 km resolution fields of modal conjugate triplets (nadir-forward-forward or  
48 nadir-aft-aft). The raw height resolved feature motion vectors reconstructed from conjugate triplets undergo  
49 flagging and quality control operations that ultimately yield the height resolved cloud motion vectors (on  
50 the regularly gridded system with 17.6 km resolution) provided to end users.  
51  
52  
53  
54  
55  
56  
57  
58  
59  
60  
61  
62  
63  
64  
65

1 The CIPS cloud tracking was carried out between two adjacent orbits (with 96 minutes time  
2 difference) with no stereo vectors being retrieved because PMC height is relatively constant, i.e.,  $83 \pm 3$   
3 km. The screening/editing strategies are designed differently but also share similarities (see section 4) with  
4 the MISR cloud tracking. For example, we have used different frame sizes rather than obtaining multiple  
5 conjugates from different cameras as in the MISR cloud tracking, to achieve redundancy of the wind  
6 detections. For the sake of quality control, we have sampled CIPS winds on two regularly spaced grid  
7 systems, i.e.,  $1.5^\circ\text{lon} \times 1.5^\circ\text{lat}$ , and  $4.5^\circ\text{lon} \times 4.5^\circ\text{lat}$ , with shifted node positions, resulting in totally five sets,  
8 to verify the consistency and robustness of the wind product.  
9

10  
11 In section 2 the AIM CIPS level-2 product and the Navy Operational Global Atmospheric Prediction  
12 System-Advanced Level Physics and High Altitude (NOGAPS-ALPHA) assimilated data set are described  
13 [Eckermann et al., 2004; 2009]. In section 3 the CIPS cloud wind tracking algorithm and screening/editing  
14 strategy are elaborated. The examples of matching results are demonstrated and discussed in section 4. In  
15 section 5 the wind product is demonstrated orbit-by-orbit, to compare with the NOGAPS-ALPHA winds at  
16 their coincidences. In section 6 the intra-seasonal variability of zonal and meridional winds (i.e., U and V)  
17 are compared between CIPS, NOGAPS-ALPHA, and Horizontal Wind Model (HWM14) wind sets [Drob  
18 et al., 2008; 2015]. In section 7 regression analysis is carried out to assess the relative importance of tides  
19 and 2-10day variability modes in the NOGAPS-ALPHA winds. The remaining issues and conclusions are  
20 summarized in sections 8-9.  
21  
22

## 23 **2. Data sets**

### 24 **2.1. CIPS level-2 PMC images**

25  
26 AIM satellite is a polar orbiting (i.e.,  $97.8^\circ$  inclination angle) sun-synchronous satellite (2007-current)  
27 that was launched into a near-circular Earth orbit at  $\sim 600$  km altitude above the Earth surface in April 2007  
28 [Russell et al., 2009]. AIM crosses the equator at 12 AM/PM local times (LTs). CIPS aboard the AIM  
29 satellite is the first PMC imaging instrument to date to obtain an extended PMC polar coverage north/south  
30 of  $70^\circ\text{N/S}$  continuously throughout the summer. The fact that AIM is polar orbiting and sun-synchronous  
31 will enable approximately the same LT crossing ( $13\text{-}22^{\text{th}}$  hour in the north) for a given lon as the orbit  
32 progresses westward. The CIPS instrument consists of an array of four cameras operating with a 15 nm  
33 passband centered at ultra-violet 265 nm and provides imagery of the PMCs against the background  $\text{O}_3$   
34 absorbed unlit atmosphere at this wavelength. Different cameras can photograph the same cloud mass with  
35 a slight time lag due to strong overlaps of images in the along-orbit direction. The CIPS horizontal  
36 resolution is approximately  $\sim 2$  km at the center of the bowtie and then is degraded to  $\sim 7$  km toward the  
37 edges. The field-of-view (FOV) of the camera system is  $80^\circ \times 120^\circ$ , centered right below the satellite, with  
38  
39  
40  
41  
42  
43  
44  
45  
46  
47  
48  
49  
50  
51  
52  
53  
54  
55  
56  
57  
58  
59  
60  
61  
62  
63  
64  
65

1 the 120° axis along the orbital track. After the removal of the Rayleigh scatter which is symmetric over the  
2 scattering angle, PMC ice particle scattering phase function is obtained assuming the knowledge on the  
3 shape and distribution of the ice particles to further retrieve the PMC albedo that is defined as the would-be  
4 albedo at solar zenith angle of 90° and therefore it only depends on the total ice component of the albedo  
5 [Bailey et al., 2009].  
6  
7  
8  
9

10 CIPS v4.20 level-2 orbital strips are used in this study. The stacks of 27 bowties each orbit are  
11 combined to produce one orbital strip with a uniform resolution of 25 km<sup>2</sup>. The background Rayleigh  
12 scatter removal is carried out for the entire strip assuming that the background O<sub>3</sub> variability does not  
13 depend on the individual pixels [Lumpe et al., 2013]. Iterations are carried out after the first guess retrieval  
14 of the ice water content until the residual Raleigh scatter approaches zero.  
15  
16  
17  
18

## 19 **2.2. NOGAPS-ALPHA winds**

20  
21  
22 The NOGAPS model with Advanced Level Physics and High Altitude (ALPHA) has extended the  
23 upper boundary to about 100 km. The NOGAPS-ALPHA included the radiative heating and longwave  
24 cooling processes with the non-local thermodynamic equilibrium effect considered, the non-orographic  
25 gravity wave drags, ozone photo-chemistry processes, and the data assimilation system (DAS) component  
26 on a 6-hourly basis. The NOGAPS-ALPHA data assimilation system (NAVDAS) component consists of  
27 the Aura Microwave Limb Sounder (MLS) v2.2 temperature and H<sub>2</sub>O in the pressure range of 32-0.01hPa  
28 [Schwartz et al., 2008], and the Sounding of the Atmosphere using Broadband Emission Radiometry  
29 (SABER) instrument on the Thermosphere Ionosphere Mesosphere Energetics and Dynamics (TIMED)  
30 satellite v1.06 temperature [Mertens et al., 2004]. Eckermann et al. [2009] used the SABER v1.07  
31 temperature up to 0.002 hPa to correct the summer mesopause region where PMCs form. Eckermann et al.  
32 [2009] also corrected the v2.2 MLS temperature toward SABER so that the known MLS cold bias in the  
33 mesopause region was reduced.  
34  
35  
36  
37  
38  
39  
40  
41  
42  
43

44 The forecast component of NOGAPS-ALPHA can provide output of the 1-hourly product with the  
45 same 6-hourly forecast-assimilation cycle [e.g., Siskind et al., 2012; Stevens et al., 2017]. The 1-hourly  
46 product includes temperature, geopotential height, and winds but does not include H<sub>2</sub>O. Unlike the 6-hourly  
47 product which is on a 360×181×60 (1° horizontal resolution) grid system, the 1-hourly product is on the  
48 240×120×74 (1.5° horizontal resolution) with the upper boundary extended from the originally 0.0005 hPa  
49 to 0.0001hPa to cover lower thermosphere. The one-hourly product is used in this study because the time  
50 coincidences can be achieved more closely and also it has a pressure grid of 0.00436 hPa which matches  
51 the PMC height more precisely than the 0.0036 hPa in the 6-hourly product.  
52  
53  
54  
55  
56  
57  
58  
59  
60  
61  
62  
63  
64  
65

1 The NOGAPS-ALPHA assimilation does not include any middle atmospheric wind measurements.  
2 Rather, the NAVDAS calculates correlated temperature and wind increments based on a gradient wind  
3 approximation. The assimilated wind and temperature fields are further constrained by the physical  
4 parameterizations of the atmospheric model (e.g., gravity wave drag, diffusion) [McCormack et al., 2009].  
5 The NOGAPS-ALPHA and the Metero radar wind measurements reach close agreement at 54°N and 88  
6 km of altitude throughout July and August 2007, which was considered beyond expectation considering the  
7 fact that no wind information is assimilated into the NOGAPS-ALPHA. Via wave analysis, Eckermann et  
8 al. [2009] found spectral peaks of westward traveling quasi-5day and 2day wavenumbers 1-2 and a strong  
9 migrating diurnal tidal component at 65°N and 0.006 hPa in both temperature and winds. McCormack et al.  
10 [2009; 2014] showed that the quasi-2day wavenumbers 3-4 are the dominant spectral peak at 40°N/S and  
11 0.01 hPa, and furthermore it shows that the high amplitude zone of this component extends toward higher  
12 latitude and altitude with a broad maximum occurred at 40°-70°N/S and 0.001 hPa. Both studies indicate  
13 widespread tidal variability and 2-10day/wavenumbers 1-4 planetary scale variability in winds,  
14 temperature, and H<sub>2</sub>O.  
15  
16

### 26 3. Algorithm

#### 27 3.1. Rationale of the matching frame-size

31 Matching frames are required to carry out the pattern matching. Before choosing the matching frame  
32 size, we resample the CIPS level-2 “push-broom” orbital images on a roughly 5 km × 5 km universal  
33 gridding system in both longitudinal (i.e.,  $\Delta\text{lon}$  enforced by 5 km) and latitudinal (i.e.,  $\Delta\text{lat}=0.05$ )  
34 directions, shown in Figure 1a. The purpose of the resampling is to precisely define the matching frame and  
35 to register the preliminary wind products on a universal spatial gridding system. A frame-size of  
36 approximately 500 km × 400 km (lon × lat) is taken as the default, which is the same as used in Rong et al.  
37 [2015]. The 500 km refers to the length in the lon direction at the low-lat limit of the frame, and it is  
38 reduced to 458 km at the central line of the frame. The maximum speed required for a movement over a full  
39 frame size within 96 minutes is approximately 80 m/s or 70 m/s in lon or lat directions, which is close to  
40 the maximum wind speeds in this altitude range. Stober et al [2012] indicates that using a running window  
41 of ~1 hour centered at the mesopause (~80-95 km) in July, the zonal winds measured by the Middle  
42 Atmosphere Alomar Radar System (MAARSY) on the island of Andøya (69.11°N, 15.76°E) fluctuates in  
43 the range of -100 m/s to 70 m/s whereas for the meridional winds the lower limit is slightly lower, reaching  
44 only -70 m/s [Renkowitz et al., 2018; Lübken et al., 2004].  
45  
46  
47  
48  
49  
50  
51  
52  
53  
54  
55  
56

57 For a given cloud feature enclosed within a frame in the current orbit, the optimum match from the  
58 next orbit is searched within one (default) frame-size of domain in all directions by an increment of 5 km.  
59  
60  
61  
62  
63  
64  
65

1 To obtain multiple winds within the current orbit, the frame is moved around by a step of every 1/3 frame-  
2 size to capture different cloud features. The 1/3 frame-size is a sufficiently small step because the wind  
3 product resolution will be no better than the frame-size itself. Smaller steps produce more redundant wind  
4 detections so that the wind field will be less fluctuating. The choice of the 1/3 frame-size is to balance  
5 between the computational efficiency and a sufficiently dense spatial coverage of the wind detections. In  
6 general a larger group of pixels represent less random cloud features and therefore will maintain better  
7 consistency between the two adjacent CIPS orbits. Better consistency between the progressive patterns  
8 points to a higher probability of successful match. On the contrary, a smaller area of clouds is less likely to  
9 be recognized after 96 minutes. The physical rationale of this argument is associated with the PMC lifetime  
10 that is not yet fully characterized or quantified so far. A smaller cloud pattern however is more likely to  
11 achieve a higher correlation with an irrelevant cloud pattern that is further away from one frame size.  
12  
13  
14  
15  
16  
17  
18  
19  
20

21 The best match of a cloud pattern is defined by the highest Pearson correlation reached, in the next  
22 orbit within  $\pm$  default frame size in both lon and lat directions. If the highest correlation of the two patterns  
23 does not exceed 0.7, then it is considered a zero match. The 0.7 threshold is empirically chosen to ensure a  
24 reasonably number of detections per day. Figure 1b shows that the wind detection number exceeds 1000  
25 per day with a standard deviation (STD) of about 200, but this number rapidly decreases as the threshold  
26 correlation coefficient increases. For example, when a 0.8 threshold is used the number of detections  
27 rapidly decreases to  $\sim$ 30%. But what is worth pointing out is that the wind detections using the 0.8  
28 threshold are not proven to be significantly more reliable, which requires a separate investigation in the  
29 future.  
30  
31  
32  
33  
34  
35  
36  
37

### 38 **3.2. A hierarchy of frame sizes**

39  
40 In the CIPS cloud wind tracking where pattern matching has a relatively low success rate due to the  
41 longer time interval, the reliability of the wind detection critically depends on two factors: one is the  
42 distance of the horizontal movement, and the other is the correlation coefficient reached. Both a smaller  
43 displacement and higher correlation coefficient will lead to more reliable detections. The high correlation  
44 ensures that they are the same cloud mass, while the smaller displacement reduces the possibility that these  
45 cloud masses resemble each other by chance. It is nevertheless not possible to entirely rule out false  
46 matches. Another factor that may impair the validity of the CIPS wind tracking is the possibility that  
47 traveling waves produce false matches due to the repeated troughs and ridges. Such cases are rare because  
48 most cloud patterns exhibit uniquely identifiable mostly irregular shapes so that the impact from waves,  
49 especially of the planetary scales, will likely be reflected by systematic changes in brightness between the  
50 96 minutes, which will be discussed in section 4.  
51  
52  
53  
54  
55  
56  
57  
58  
59  
60  
61  
62  
63  
64  
65

1 A hierarchy of three frame sizes, 0.75×default size, default, and 1.25×default size, are adopted to  
2 carry out three sets of pattern matching calculations. The main purpose of adopting three frame sizes is to  
3 construct a redundant and eventually merged set of winds. Twenty-five percent of the frame size change  
4 does not alter the fact that they all belong to a size range that far exceeds the pixel size and that encloses a  
5 cloud pattern that most likely will remain recognizable after the 96 minutes given some degree of variation.  
6 In the previous PMC model studies the PMC lifespan can reach up to 24-48 hours [e.g., Jensen and  
7 Thomas, 1988; Rapp et al., 2002], which is many times longer than the 96 minutes and will support the  
8 validity of cloud tracking. While in practice PMCs appear to change more rapidly due to temperature and  
9 H<sub>2</sub>O variability. Nevertheless, Rong et al. [2015] showed that between adjacent CIPS orbits the PMCs with  
10 brightness change by 50% within the same frame location, either halved or doubled, take up only ~15% of  
11 the cloud population. This will indirectly support a significant degree of stability in the PMC patterns  
12 between the 96 minutes.  
13  
14  
15  
16  
17  
18  
19  
20  
21  
22

23 To further explore the PMC pattern stability, or “memory”, over the 96 minutes, we next characterize  
24 each frame size with a histogram of the correlation coefficients at the same frame locations and then  
25 register each coefficient with a wind speed assuming wind advection is the sole mechanism of variability,  
26 which is shown in Figure 2. The correlation coefficient would have a one-to-one correspondence to the  
27 displacement of a cloud pattern if the dominant spatial scale is wavenumber-1 in a sinusoidal form and the  
28 wind advection is the sole mechanism to drive the cloud pattern variation. The large scale dominance over  
29 smaller scales within a 400-500 km frame is proven to be the case in the CIPS clouds in Rong et al. [2018].  
30 The bottom x-axis is the correlation coefficient which varies from +1 to -1, corresponding to the sinusoidal  
31 phase shift from zero to 180°. The wind speed corresponding to the correlation coefficient of -1 provides a  
32 more stringent upper limit for the winds because it corresponds to a half frame-size movement. The wind  
33 speeds registered at the top x-axis are the mean values within each bin with non-zero correlation  
34 coefficients from the actual CIPS analysis. Three arbitrarily selected days in the summer of 2007 are used  
35 to explore this statistics.  
36  
37  
38  
39  
40  
41  
42  
43  
44  
45  
46

47 Figure 2a indicates that for the frame-size of 125 km, about 54% of cloud population appears to  
48 possess a memory of the original pattern via showing a positive correlation. Statistically it points to a  
49 mildly positive but virtually zero memory, and therefore the wind speed at the top x-axis is not much  
50 indicative. Some of the positive correlation coefficients could have been achieved randomly because cloud  
51 features enclosed in smaller frames are prone to higher correlation. The 125 km frame-size is therefore not  
52 an appropriate one to use in the CIPS wind tracking. The memory is increasingly improved as the frame  
53 size increases. For example, for the frame size of 625 km, 79% of the cloud population has a positive  
54 correlation with the original pattern. The largest wind speed registered at non-zero bins of the histograms  
55  
56  
57  
58  
59  
60  
61  
62  
63  
64  
65

1 are about 25 m/s, 30 m/s, and 35 m/s for the frame sizes of 375 km, 500 km, and 625 km respectively. The  
2 wind speed thresholds yielded for the three frame sizes are in terms of the full velocity speed  $\sqrt{U^2+V^2}$   
3 where U and V are zonal and meridional velocities. These thresholds are adopted to generate a subset of  
4 winds, or so called “more reliable” winds, to inspect the cloud tracking results from a different perspective.  
5  
6 But we should point out that CIPS cloud wind tracking, even without these newly registered thresholds,  
7  
8 may succumb to a bias toward smaller zonal winds because the result is not reliable for longer distance  
9  
10 displacement. While Renkwitz et al. [2018] have shown that the westward winds in the polar summer  
11  
12 mesopause region exceed 100 m/s in many occasions.  
13  
14

15 This analysis implied that we should choose larger frames since they possess better memory after 96  
16 minutes, but a larger frame will technically reduce the number of wind detections because we will have  
17 fewer independent cloud features. In addition, an indefinitely larger frame will embrace more complex  
18 cloud features that are driven by inhomogeneous cloud physics or dynamics, which will reduce the success  
19 rate of the pattern matching and also eventually reduce the number of the wind detections. This later point  
20 however cannot be verified because we are unable to examine sizes much greater than 750 km due to the  
21 fact that the cross-orbit width of the CIPS orbital strip is ~800 km [Lumpe et al., 2013].  
22  
23  
24  
25  
26  
27

### 28 **3.3. Screening/editing strategies**

29  
30  
31 In order to apply the screening/editing procedure we first merge the preliminary wind products from  
32 using the three frame sizes. Upon merging the preliminary wind products from the three frame sizes the  
33 horizontal spacing is reduced to roughly 114 km  $\times$  100 km corresponding to 1/3<sup>rd</sup> of the frame size 375 km.  
34  
35 The merged winds will be eventually resampled on the NOGAPS-ALPHA 1-hourly product grid system  
36 (1.5°  $\times$  1.5°) and a grid system three times coarser. The 1.5° lon and lat bin-size north of 70°N (i.e., 57 km  
37  $\times$  167 km at this latitude) is adopted to conveniently compare with the NOGAPS-ALPHA winds.  
38 Remember that the spatial increment of the wind tracking calculations is 1/3 of the frame size in both lon  
39 and lat directions and therefore the preliminary CIPS wind product spacing is roughly 153 km  $\times$  133 km for  
40 the default frame size, where “153 km” is the length in the lon direction along the central line of the frame.  
41  
42 This spacing is comparable to the spatial resolution of the NOGAPS-ALPHA winds. The coarser grid  
43 system of 4.5°  $\times$  4.5° is used because it is close to the actual spatial resolution of the wind product.  
44  
45  
46  
47  
48  
49  
50

51  
52 After choosing the sampling grid-size, different nodes are used. In the 1.5°  $\times$  1.5° (lon  $\times$  lat) case we  
53 use two types of nodes, one is the original NOGAPS-ALPHA 1-hourly grid system, and the other is the  
54 NOGAPS-ALPHA grid with a half grid-size shift. In the 4.5°  $\times$  4.5° (lon  $\times$  lat) case three nodes are used,  
55 zero-shifted, 1.5° shifted, and 3° shifted, respectively. Different sampling grids along with different nodes  
56 are used to rule out any possible uncertainty induced by a specific sampling process.  
57  
58  
59  
60  
61  
62  
63  
64  
65

1 The screening/editing strategy is required within each sampling grid because winds can be  
2 contradictory due to the false matches caused by the inherent limitation of the wind tracking approach.  
3  
4 Within the sampling grid we first divide the winds into clusters with each cluster possessing two or more  
5 wind values and the directional difference for each pair of these winds being smaller than 20°. Any  
6 individual wind that does not pair up with any other wind in the sampling grid-cell is removed. On the  
7 contrary, if any individual wind is involved in many different pairs then its value will be closer to being  
8 representative to the mean wind within the given sampling grid-cell. The clusters of winds are then  
9 averaged to create the mean wind of the sampling grid-cell. If there is no pair at all, the minimum wind will  
10 be selected as the value of the sampling grid-cell since a small displacement is considered more reliable in  
11 the CIPS cloud tracking. In many cases this approach will virtually exclude any singular winds that are  
12 drastically different from the rest of the winds within a given sampling grid-cell. But to implement the  
13 approach to its fullest extent we must have highly redundant winds within a given sampling grid-cell which  
14 is not yet the case unless wind tracking is carried out by a step much smaller than 1/3<sup>rd</sup> of frame-sizes.

#### 24 **4. Elaboration of three pattern matching examples**

27 In order to gain a tangible understanding of the CIPS cloud pattern match, Figure 3 shows examples  
28 of using the three frame sizes respectively. The selected matches are characterized by speed values  
29 ( $\sqrt{U^2+V^2}$ ) that are very close to 25 m/s, 30 m/s, and 35 m/s which are the wind thresholds in the  
30 constrained cases. The Figure 4 that follows shows the corresponding images that are exactly enclosed in  
31 the frames so that we are able to further examine the similarity of the cloud structures between the two  
32 CIPS orbits.  
33  
34  
35  
36  
37

38 In all three panels of Figure 3 we discovered some degree of sudden increase of overall brightness  
39 between two orbits both inside and outside the matching frames, which may have stemmed from the larger  
40 scale wave effect, i.e., 2-5day planetary waves or tides, in temperature or H<sub>2</sub>O. For example, a 2day wave  
41 would travel about ~350 km within 96 minutes at 75°N, which is a sufficiently long distance to cause  
42 systematic temperature change within the frame. It is also worth pointing out that such a sudden change of  
43 cloud brightness between adjacent orbits is a regular occurrence in CIPS and may be worth a separate  
44 investigation. The brightness change however does not directly affect the pattern matching result because  
45 the recognizable irregular pattern shape serves as the identity of a cloud mass, i.e., in Figure 3a it is drifted  
46 upper-left (or north-west) and in Figure 3b it is mostly toward the left (or west). In Figure 3c there are signs  
47 of straight wave structures outside of the matching frames indicated by the red dashed lines and the  
48 orientation of the waves appear to have slightly changed between two orbits. It is unclear how much gravity  
49 wave propagation could have contributed to the variability on the later orbit. It could have been that the  
50 entire cloud mass turned brighter and meanwhile was drifted south-west. This could very likely be the case  
51  
52  
53  
54  
55  
56  
57  
58  
59  
60  
61

1 based on the prediction by Fogle and Haurwitz [1966]. Another noteworthy feature, which has occurred  
2 more than occasionally in the CIPS PMCs, is that the semi-organized small scale (e.g., wavelength of ~20-  
3 60 km) wave structures within the frame suddenly become either more or less distinct on a later orbit (after  
4 96 minutes) without any clear indication of propagation. Revisiting the detailed small scale gravity wave  
5 structures in Figure 4b we find that the “lattice” shaped interfering wave structures are present on both  
6 orbits but in the later time frame they appear more distinct. We will in the future examine how these pairs  
7 of wave structures differ in a statistical sense in the CIPS cloud tracking frames and what mechanism  
8 controls their evolution.  
9

## 15 **5. Coincidence analysis with the NOGAPS-ALPHA winds**

### 18 **5.1. Demonstrate the agreements at the coincidences**

20 We next will use the NOGAPS-ALPHA 1-hourly winds, NOGAPS hereinafter, on the pressure  
21 surface of 0.00436 hPa (~84 km) to compare with the CIPS cloud tracking winds. NOGAPS is adopted as  
22 the first data set to assess the CIPS wind tracking product because it is available on a regular gridded  
23 system (1.5°lon×1.5°lat) with the full 3-D coverage throughout the 2009 summer so that coincidences exist  
24 for all individual CIPS winds. It has been used in several previous PMC studies such as in Stevens et al.  
25 [2010; 2017] but their main focus was not in the very high latitude range such as 70°-86°N. The following  
26 analysis is a mutual assessment process to examine the consistency between the CIPS and NOGAPS in a  
27 broad spectrum. The NOGAPS is a combination of the model prediction and DAS system. The model  
28 included the radiative heating and cooling and the gravity wave drag to be able to resolve tides and other  
29 planetary scale variability along with the meridional circulation.  
30

31 Prior to the wind comparison we first examine whether the NOGAPS zero-dimensional (0-D)  
32 modeled ice [Hervig et al., 2009] and the CIPS ice reasonably agree in a statistical sense, which serves to  
33 examine the more fundamental consistency between CIPS and NOGAPS. We have learnt that in NAVDAS  
34 temperature and wind increments are linked to each other via gradient wind approximation. Temperature  
35 also plays a strong role in the 0-D model in which super-saturation immediately results in the ice  
36 production and the full amount of H<sub>2</sub>O in excess of the frost point is turned into ice.  
37

38 For each orbit per day we have used the NOGAPS temperature and H<sub>2</sub>O at the coincident  
39 lons/lats/universal time (UT) (with CIPS) to carry out the 0-D calculations throughout the whole season,  
40 and a roughly 5 K correction toward warmer state is applied to the NOGAPS temperature to alleviate the  
41 known cold bias [Stevens et al., 2017]. Over each orbit a spatial correlation coefficient between the CIPS  
42 measured ice and the NOGAPS 0-D ice is calculated.  
43  
44  
45  
46  
47  
48  
49

1 The histogram of the coefficients (shown in Figure 5a) indicates that the positive correlation  
2 dominates but there is a significant fraction of negative coefficients which point to poorly correlated 0-D  
3 ice and CIPS ice in these particular cases. A closer examination to specific pairs (not shown here) indicates  
4 that in many cases, i.e., with weak positive correlations for example, larger scale zonal variabilities of the  
5 NOGAPS 0-D ice and the CIPS ice roughly agree but this does not ensure high positive correlation since  
6 the CIPS ice exhibits stronger cascading toward smaller scale features compared to the 0-D ice. In some  
7 cases especially, the variability patterns agree over only a fraction of the zonal circle. The red colored  
8 histogram in Figure 5a indicates that the 0-D ice holds a strong anti-correlation with (the NOGAPS)  
9 temperature and therefore temperature almost entirely controls the 0-D ice variability.  
10

11 Figure 5b shows the daily time series of the correlation coefficients between the CIPS measured and  
12 0-D modeled ice, confirming the overall weak but definitely positive correlation and furthermore the  
13 leading three largest coefficients are distinctly higher. The imperfection of the NOGAPS temperature could  
14 be one of the main causes for the discrepancy between the 0-D ice and CIPS ice, probably due to the  
15 NOGAPS model physical constraint and the accommodation between the MLS and SABER measured  
16 temperature in the DAS component that is incorporated on a 6-hourly basis.  
17

18 The CIPS wind detections are overlapped on the CIPS PMC albedo map on the orbit close to the UT  
19 hour 21, on DOY 185 of 2009, to demonstrate the sanity of the cloud tracking result, shown in Figure 6.  
20 We should point out that in this display the zonal and meridional winds used the same scale but due to the  
21 ratio of the display the meridional winds appear dominant. In practice the zonal winds should be about 5-  
22 times stronger than what is observed here, as shown in the legend. The CIPS winds determined using these  
23 two orbits are toward north-west and south-west directions respectively split at longitude of  $30^{\circ}\text{W}$ ,  
24 indicating reversed meridional wind directions between the two lon sections. The albedo distribution  
25 roughly echoes such a directional move of clouds although the cloud brightness is notably strengthened in  
26 the later orbit. The brightness change was argued to be caused by tides or planetary waves.  
27

28 The wind agreement and discrepancy at the CIPS and NOGAPS coincidences for the same orbit are  
29 shown by different colors in Figure 7. The agreement here refers to both the zonal and meridional winds  
30 having consistent directions between the two wind sets. In the longitudinal section  $100^{\circ}\text{W} - 30^{\circ}\text{W}$ , both  
31 CIPS and NOGAPS echoed a westward and poleward flow. In the longitudinal section of  $30^{\circ}\text{W} - 10^{\circ}\text{E}$  the  
32 agreement with NOGAPS is much poorer with only one value being consistent (see Figure 7a and 7b). In  
33 Figure 7c the full NOGAPS wind vector field at the same UT hour is overlapped on the geopotential height  
34 field, which demonstrates that the NOGAPS winds are roughly geostrophic since the left (or right) side of  
35 the winds is nearly always characterized by lower (or higher) geopotential height. From Figure 7c we can  
36 see that the reversal of the meridional winds did also occur in the NOGAPS winds but in a further down  
37

1 longitudinal section of 0-100°E due to the less rapid variability along the zonal circle. Such a phase  
2 difference is noted often in both ice and winds between CIPS and NOGAPS. Several factors may contribute  
3 to the potential discrepancies; first, the NOGAPS temperature deviates from the true temperature which  
4 would affect the geostrophic winds; second, the CIPS winds capture a larger abundance of smaller scale  
5 variabilities which are ageostrophic in nature. Figure 7 overall also indicates in both CIPS and NOGAPS  
6 results the wind directions are roughly consistent over a large part of 70°- 86°N, pointing to a relative weak  
7 latitudinal variability of the winds.  
8  
9

10  
11  
12  
13  
14 The wind agreements at the coincidences throughout all orbits (or UT times) for the same DOY 185  
15 2009 (Figure 8) suggest that they are widespread but are unbalanced in numbers between different orbits.  
16 The generally consistent westward directions over the different orbits point to the existence of the  
17 migrating tides in the zonal winds or a genuine zonal mean easterly, while the frequent reversals of the  
18 meridional wind directions suggest that either higher frequency of tides or non-migrating tides may have  
19 contributed significantly.  
20  
21  
22  
23

## 24 **5.2. Statistics of the full season**

25  
26  
27 We next examine the statistics of the agreements throughout all the summer DOYs in 2009. Figure 9  
28 shows the scatter plots of total number of CIPS winds per day versus number of agreements with  
29 NOGAPS, with and without wind speed thresholds applied. For each day all wind detections are included  
30 regardless of the orbits/UT times. It shows that if we focus on the zonal or meridional winds only, the  
31 fraction of agreement exceeds 50% by 1-6% at the coincidences. When both zonal and meridional winds  
32 are required to be consistent between CIPS and NOGAPS, the fraction of agreement exceeds 25% by 4-6%.  
33 Both percentages indicate that averaging over all orbits there is still a modest degree of deterministic  
34 consistency between the CIPS and NOGAPS winds. It is also worth mentioning that the “reliable” winds  
35 with thresholds applied show qualitatively the same but slightly better result which is not sufficient to  
36 conclude that that more accurate cloud wind tracking will improve the degree of agreement.  
37  
38  
39  
40  
41  
42  
43  
44  
45

46 The CIPS winds and NOGAPS winds do not show consistently 29-31% of agreement on all  
47 orbits/UT times. Rather, the percentage is highly unbalanced between orbits. The same asymmetry between  
48 orbits is also shown in the ice comparison in Figure 5b. We suspect that on some orbits CIPS and NOGAPS  
49 may maintain better consistency in both ice distribution and wind directions. Figures 10a-b show the intra-  
50 seasonal variability of the leading three higher agreement numbers (per orbit) divided by the median  
51 agreement numbers (per orbit). The spikes of the ratio reaches 10 which suggests that the numbers of the  
52 CIPS and NOGAPS wind direction agreements are much higher on the three out of the 14 orbits. In Figure  
53 10b when the agreement criterion tightens to a 10° of directional difference the result is qualitatively the  
54  
55  
56  
57  
58  
59  
60  
61  
62  
63  
64  
65

1 same except that the asymmetry between orbits becomes stronger, further confirming the unbalanced  
2 numbers of wind agreements between orbits.  
3

4 To further quantify the relationship between the ice distribution consistency and the wind direction  
5 agreement, we pair up the ice correlation coefficient and wind agreement number for each orbit on a daily  
6 basis and do find a positive slope even though a fairly large scatter exists, shown in Figure 10c. The slope  
7 is larger for the stricter 10° criterion case indicating a more distinct relationship between the ice distribution  
8 consistency and wind agreement number. Such a relationship exists probably because both the NOGAPS 0-  
9 D ice and geostrophic winds are associated with temperature. The large scatter suggests that other factors  
10 are in play such as the inherent limitation of cloud tracking approach and the ageostrophic nature of the  
11 CIPS winds.  
12  
13  
14  
15  
16  
17  
18

## 19 **6. Intra-seasonal variability of the winds**

20 The global general circulation in the mesosphere is transitioned into distinctly different states  
21 between different seasons [Garcia and Solomon, 1985], reflected by the clockwise to anti-clockwise  
22 reversal of the residual circulation between hemispheres from summer to winter. As a result, we would  
23 expect weakened westward or equatorward winds at the start and end of summer. Due to the generally poor  
24 spatial and temporal data coverage of wind measurements, to this date the detailed intra-seasonal variability  
25 in the polar region for individual years has rarely been discussed. The monthly climatology at the PMC  
26 height indicates that zonal (westward) winds accelerate throughout April, May and June, reach the  
27 maximum prior to mid-July, and then decelerate in August and further are rapidly reversed to eastward  
28 winds in September [Portnyagin et al., 2004b; Dowdy et al., 2007; Lukianova et al., 2018].  
29  
30  
31  
32  
33  
34  
35  
36  
37  
38

39 The spatial and temporal sampling condition of the CIPS winds is the first aspect to understand in  
40 order to further examine any daily mean behavior of these winds since it may greatly affect the magnitude  
41 and variability of the winds. The CIPS LT coverage in three representative days, DOYs 152, 183, 214 of  
42 2009, are shown in Figure 11a which indicates a consistent and continuous coverage in the range of 13-22  
43 LT hours, suggesting that CIPS only covers the 2<sup>nd</sup> half of the day in the northern polar summer. If tidal  
44 variability is strong (see section 7) this may serve as a key factor to constrain the overall magnitude of the  
45 CIPS zonal winds. Figure 11b shows that in both 2009 and 2007 the daily mean latitudes of the CIPS winds  
46 remain fairly constant by staying at 81°N or slightly higher but toward the start and end of the season the  
47 fluctuation becomes stronger suggesting more uncertainty stemming from smaller number of wind  
48 detections. There is a fairly broad standard deviation (STD) of 1.9° reflecting the fact that the wind  
49 detections are widespread north of 75°N. The slight differences between the years 2009 and 2007 do not  
50 substantially affect the intra-seasonal variability of the winds because the latitudinal gradient of hourly  
51  
52  
53  
54  
55  
56  
57  
58  
59  
60  
61  
62  
63  
64  
65

1 NOGAPS horizontal wind field is generally small and moreover such a gradient is not consistent  
2 throughout the day (not shown here), which would prevent a systematic impact on the daily mean values.  
3

4 The daily mean time series of the CIPS zonal winds in the 2009 and 2007 polar summers and the  
5 NOGAPS winds on the coincidences (with CIPS winds) are shown respectively in Figure 12. The  
6 NOGAPS winds are sampled at both years' coincidences to explore whether the intra-seasonal variability is  
7 susceptible to the small changes in the sampling lons and lats. Universally in all cases in Figure 12 the  
8 westward winds prevail with widespread transient day-to-day fluctuation. The 2<sup>nd</sup>-order polynomial fitting  
9 curves exhibit distinct acceleration and deceleration of the westward winds in early June and late August in  
10 both years in CIPS winds although short excursions of larger winds can occur at both the start (i.e., in  
11 2007) and end (i.e., 2009) of the season creating asymmetry in the polynomial fit. The approximate timing  
12 when seasonal maximum zonal wind is reached is in early to middle July which approximately agrees with  
13 what Lukianova et al. [2018] has shown over the years 2009-2015. Generally speaking the timing when  
14 maximum zonal wind is reached could be dependent on year or lon/lat [also see Dowdy et al., 2007]. The  
15 CIPS intra-seasonal variability differs from the several climatology studies (cited above) in the sense that it  
16 has a much earlier reversal of the prevailing zonal wind direction in the beginning of the summer. The daily  
17 mean CIPS zonal wind reaches seasonal maximum of ~15-20 m/s with the standard error of the mean  
18 (SEM) staying within ~1.5 m/s on average suggesting an uncertainty that is far below the actual magnitude  
19 in most cases. However toward the start and end of the season, due to the smaller numbers of wind  
20 detections, the SEM could reach 7-10 m/s (not shown here) suggesting poorer reliability of the daily mean  
21 winds during these times.  
22  
23  
24  
25  
26  
27  
28  
29  
30  
31  
32  
33  
34  
35  
36

37 The CIPS wind subset with smaller speeds comprises about 30% of the CIPS wind detections, and the  
38 polynomial fit indicates an almost constant level of zonal winds throughout the season with no distinct  
39 intra-seasonal variability except that in August 2007 the decrease of the westward winds and wind reversal  
40 is notable. Although the subset does not capture the intra-seasonal variability shown in the full set due to  
41 the more strongly constrained maximum wind speed, the correlation between the two daily time series  
42 reaches a fairly high correlation of 0.5-0.6 reflecting a significant degree of self-consistency on the day-to-  
43 day variability. We also rely on this self-consistency to remove the days at the start and end of the season  
44 during which the day-to-day variability patterns of the full set and subset notably contradict each other. As  
45 a result the length of daily time series slightly varies with year.  
46  
47  
48  
49  
50  
51  
52  
53  
54

55 The NOGAPS zonal winds at the (CIPS wind) coincidences show drastically different intra-seasonal  
56 variability characterized by stronger westward winds throughout the season. This is expected since in  
57 NOGAPS the timings of the seasonal wind reversal are extended back into May or April depending on the  
58 LT ranges. It is especially noteworthy that the NOGAPS zonal winds are strengthened in August relative to  
59  
60  
61  
62  
63  
64  
65

1 June and July, which is not echoed in the CIPS result or in the wind climatology [Portnyagin 2004b;  
2 Lukianova et al., 2018]. As Eckermann et al. [2009] has stated, tuning the gravity wave drag can  
3 significantly affect the mean and tidal structures which may be able to interpret this bias but there does not  
4 seem to be an apparent anomaly in temperature or geopotential height gradient associated with the larger  
5 August winds. It is also worth mentioning that the NOGAPS zonal winds sampled at the 2009 and 2007  
6 CIPS coincidences hold a correlation of 0.7 which suggests that the zonal wind variability is only mildly  
7 affected by the sampling details reflecting a robust intra-seasonal variation pattern.  
8  
9

10  
11 The results for the meridional winds are shown in Figure 13. The 2<sup>nd</sup> order polynomial fitting curves  
12 suggest 2-5 m/s of outflow from the pole in the core of the season which is qualitatively consistent with the  
13 climatology. It is especially striking to note that the variability patterns in the CIPS meridional winds differ  
14 so drastically between 2007 and 2009; in 2009 there are smaller (meridional) winds in the middle of the  
15 season than toward the start and end; in 2007 it is the opposite. The CIPS wind subsets with smaller  
16 magnitudes show qualitatively the same results as in their full sets; in 2009 however, a large discrepancy  
17 exists in the beginning of June which worsens the correlation between the two curves to about 0.4,  
18 otherwise they agree well throughout July and August. This correlation reaches 0.7 in 2007, reflecting the  
19 excellent consistency between the full wind set and the subset.  
20  
21

22  
23 The NOGAPS meridional winds sampled at the 2009 and 2007 CIPS wind coincidences yield the  
24 same inter-annual difference, which is not expected. We so far have not identified any mechanism that  
25 would support this consistency since the NAVDAS component assimilated the satellite data in 2009  
26 exclusively. In this particular case however, the difference in NOGAPS is caused by the coincidences  
27 residing on the ascending and descending parts of the orbits respectively in the two years; we are aware that  
28 CIPS orbits in 2009 and 2007 approximately repeat, but the ascending and descending nodes are located in  
29 different longitudinal sections. Unlike in the zonal winds, the daily time series of the NOGAPS meridional  
30 winds sampled at the 2009 and 2007 coincidences show a weak correlation of 0.2, reflecting the strong  
31 impact of the sampling details in the meridional winds. The NOGAPS analysis so far indicates that the  
32 intra-seasonal variability of the meridional winds is susceptible to different sampling path and therefore  
33 does not conform to an established pattern. In the zonal winds, on the other hand, although the sampling  
34 difference from day-to-day also causes the daily value to change it is not sufficient to alter the longer term  
35 intra-seasonal variability.  
36  
37

38  
39 Partial LT coverage is considered a major cause of the overall weaker CIPS zonal winds. To  
40 elaborate this, we presented the intra-seasonal variations of the NOGAPS zonal winds in the CIPS LT  
41 range and the full 0-24 hour LT range in Figure 14. All grid points on the surface of 0.00436 hPa in the  
42 latitudinal range of 70°-86°N are used in this analysis. It is striking to note that the winds sampled at the  
43  
44

1 13-22 hour LT range are systematically weaker by about 8-10 m/s throughout the season, with the daily  
2 variability kept almost intact. This will partially interpret the overall smaller zonal winds in the CIPS wind  
3 set and also indicates that with only half of the LT coverage the zonal wind intra-seasonal variation pattern  
4 is not affected. The polynomial fitting curves suggest very mild acceleration/deceleration in early June and  
5 late August, confirming that NOGAPS zonal winds are persistently strong in these months. The uncertainty  
6 in the NOGAPS daily time series of the zonal winds reaches ~1.5 m/s reflecting the same degree of spatial  
7 variability as in the CIPS winds. In addition, the 2-10day variability in the time series with amplitude of  
8 roughly ~10 m/s reflect the wave-zero low frequency fluctuation modes since both spatial variability and  
9 tides are eliminated by the averaging process.

10  
11 The NOGAPS meridional winds in the two LT ranges (in Figure 14b) exhibit highly suppressed daily  
12 fluctuation amplitudes with the wind speed remaining almost constant at 2-3 m/s throughout the season.  
13 This reflects the strong cancellation of different variability modes in the meridional winds. Given the  
14 suppressed amplitude, the daily time series at the two LT ranges achieve a correlation coefficient of 0.5  
15 reflecting a significant degree of self-consistency probably because their spatial sampling remains the  
16 same. Given the small differences between the two curves, the longer term intra-seasonal variation patterns  
17 of the two LT ranges are qualitatively different; in the middle of the season the wind is about 1.0 m/s  
18 smaller in the CIPS LT range, whereas the values converge at the start and end of the season.

19  
20 We next briefly compare the CIPS winds with the Horizontal Wind Model 2014 (HWM14) [Drob et  
21 al., 2015] climatology. The HWM models are primarily utilized in the studies of the Earth upper  
22 atmosphere and are not much referenced in the mesospheric studies. Nevertheless the quiet time component  
23 of HWM provides the climatological horizontal winds from the ground to the exobase (~500 km altitude)  
24 as a function of day of year, solar local time, colatitude, and longitude. The atmosphere's dominant  
25 recurring cyclical climatological variations, i.e., predominantly seasonal and diurnal, are represented by  
26 height-modulated vector spherical harmonic basis functions. The HWM experienced a sequence of earlier  
27 versions such as HWM87, 90, 93, and 07. The HWM07 [Drob et al., 2008] and HWM 14 share the same  
28 observational database for winds below the mesopause, among which UARS HRDI [Hays et al., 1993],  
29 sounding rockets [Schmidlin et al., 1985], and medium-frequency radar [Murayama et al., 2000] were the  
30 listed data sets used to construct the winds in the northern PMC region.

31  
32 The HWM14 zonal winds averaged daily in the latitude range 70°-86°N exhibit a prolonged  
33 acceleration throughout June to mid-July and a deceleration in the remaining of the season. The intra-  
34 seasonal variability is more distinct than in the NOGAPS zonal wind polynomial fit. But it is especially  
35 enlightening to observe that the daily time series using all local times and using only the 13-22 hour LT  
36 range are shifted by ~6-8 m/s consistently throughout the season while sharing extremely similar intra-  
37  
38  
39  
40  
41  
42  
43  
44  
45  
46  
47  
48  
49  
50  
51  
52  
53  
54  
55  
56  
57  
58  
59  
60  
61  
62  
63  
64  
65

1 seasonal variation pattern. This LT dependence strongly agrees with the NOGAPS result, verifying that LT  
2 range is a key factor to determine the magnitude of the zonal winds, and both point to the dominant impact  
3 of the diurnal migrating tides. The overall zonal wind magnitude in the HWM14 is about ~5-7 m/s larger  
4 than the polynomial fits of the CIPS zonal winds. Although the HWM14 zonal winds show distinct  
5 asymmetry between June and August, this condition changes when the altitude surface is chosen to be at 80  
6 km or 85 km, indicating that it is not a robust feature.

7  
8  
9  
10  
11 The HWM14 meridional winds in Figure 14b show qualitatively different results between the two LT  
12 ranges, characterized by the reversed signs between the two time series prior to late July and drastically  
13 different intra-seasonal variation patterns. Although having opposite directions, both HWM14 and  
14 NOGAPS meridional winds in the LT range 13-22 hour maintain fairly constant speeds throughout the  
15 season. The condition of HWM14 consistently picking up the northward winds in the CIPS LT range is  
16 caused by the dominant migrating tides in the model (not shown here). On the contrary, in the NOGAPS  
17 meridional winds the LT dependence strongly varies between the different lons, reflecting the presence of  
18 many other scales including the non-migrating tides.

## 26 **7. Planetary scale wave analysis to the NOGAPS winds**

27  
28  
29 Regression analysis is not applied to CIPS winds because the data coverage is too poor to resolve  
30 tides which are considered the dominant variability modes [e.g., Stober et al., 2012]. The asynoptic  
31 coverage of satellite orbits will result in aliasing of the (non-migrating) tidal variability onto the 2-5day  
32 variability in the intra-seasonal time series [e.g., Salby, 1982; Talaat and Lieberman, 1999]. Polar summer  
33 mesosphere is under control of a wide spectrum of the planetary scale slow waves and tides, and these  
34 variability modes are thought to be excited by the winter polar night jet instability and the further wave  
35 ducting activity [Garcia et al., 2005]. Merkel et al. [2009] shows that CIPS PMC albedo analysis indicates  
36 multiple peaks with the westward traveling 5day wavenumber-1 and eastward traveling 2day wavenumber-  
37 1 as the dominant components. Other components such as 2day and 5day wavenumber-2 are also present.

38  
39  
40 Although a full analysis on the planetary scale waves is beyond the scope of this study, unraveling the  
41 relative importance of the tides and the 2-5day variability serves to assess the NOGAPS polar summer  
42 winds from a different perspective. We have chosen three lats (i.e., 75°N, 80°N, and 85°N) and four lons  
43 (0°, 90°E, 180°, 90°W) to generate totally 12 lons/lats in the NOGAPS winds on the 0.00436 hPa surface to  
44 extract the time series at each horizontal grid and then apply the regression analysis to each 10-day period  
45 throughout the season. Throughout June, July, and August, regression analyses are applied to the  
46 consecutive 10-day periods, with 1-day increment, to identify the amplitudes of diurnal to quarterly-  
47 diurnal, and 2-10day components. For each hourly field, winds north of 70°N are averaged since the

1 NOGAPS hourly wind field's latitudinal variability is shown to be small in many cases. A demonstration of  
2 the decomposed 10-day hourly series of zonal and meridional winds (U and V) at a selected lon/lat is  
3 shown in Figure 16. We can see that in both U and V the tidal variability and the 2-10day variability are  
4 each able to restore the total variability to a notable extent, and in almost all cases the relative mean  
5 amplitudes of the two frequency groups are 60% versus 40% based on the fraction of variances they  
6 contribute to. This suggests that tidal modes are dominant but they are clearly modulated by the longer time  
7 variability that also possesses non negligible amplitudes.  
8  
9  
10  
11  
12  
13

14 The diurnal and semidiurnal tidal amplitudes (Figures 17a and 17b) are roughly comparable varying  
15 in the range of 8-12 m/s staying fairly constant throughout the season. In the meridional winds both  
16 components are slightly smaller, by 2-3 m/s in amplitude but the intra-seasonal variability of both tidal  
17 components are similar between U and V, showing slightly larger diurnals tides in June and August while  
18 in July the semidiurnal tides are larger. The STD over the 12 lons/lats reaches 5-10 m/s reflecting a fairly  
19 large variability between different spatial points. This level of amplitude at the PMC height, for both U and  
20 V, is very similar to what is derived from the long record of the meteor radar measurements at 67°N by  
21 Lukianova et al. [2018].  
22  
23  
24  
25  
26  
27  
28

29 The mean amplitudes of the 2day and 5day variability modes stay in the range of 4-6 m/s in most  
30 cases which is about halved from the tidal amplitudes. The amplitude of the 5-day mode is substantially  
31 larger in early June in both U and V otherwise it does not show any distinct intra-seasonal variability, and  
32 the 5day variability mode is stronger than the 2day variability mode in most cases except for a short period  
33 in late June in V.  
34  
35  
36  
37

## 38 **8. Remaining issues**

39  
40  
41 The CIPS wind product is fairly robust, reflected in the daily time series of zonal winds using the  
42 1.5°×1.5° and 4.5°×4.5° sampling grids respectively in Figure 18. Although the overall wind population is  
43 halved in the coarser sampling grid their intra-seasonal variation patterns are tremendously consistent with  
44 noteworthy magnitude differences, suggesting that the preliminary CIPS wind set has achieved sufficient  
45 redundancy after merging the products from using the three frame sizes. We may in the future increase the  
46 redundancy through further splitting the 1/3 frame-size step into finer steps to examine whether it will  
47 improve the accuracy of the wind product.  
48  
49  
50  
51  
52  
53

54 The stereoscopic parallax is considered a minor error source to the CIPS winds because cloud height  
55 uncertainty is small ( $\pm 3$  km) [Russell et al., 2010] and in the meantime the time interval between the two  
56 progressive patterns is long (96 minutes). The height uncertainty will affect the wind determination through  
57 affecting the lon and lat registration. The retrieved lons and lats are included in the CIPS level-2 data, and a  
58  
59  
60  
61  
62  
63  
64  
65

1 separate investigation is required to determine the extent to which the parallax will affect the lon and lat  
2 registration given the cloud deck height varying by  $\pm 3$  km.  
3

4 The primary uncertainty in the CIPS wind tracking lies in the fact that 96 minutes are a fairly long  
5 time period so that the wave dynamics will cause variations in the PMC ice mass and further affect the  
6 pattern recognition. In fact this is the main reason why the CIPS cloud pattern matching has a relative low  
7 success rate (see Figure 1b). We argued above that between two adjacent CIPS orbits the pattern could be  
8 roughly conserved but the overall brightness level is changed due to large scale waves. Unique shape of the  
9 cloud pattern serves as identification of a cloud mass despite the large scale wave effect. But future  
10 validation is still required to further assess whether the long term operation of the CIPS PMC tracking is a  
11 worthwhile endeavor.  
12  
13  
14  
15  
16  
17  
18

19 Future cloud wind tracking should also include the pre-screening of the cloud features [Mueller et al.,  
20 2013]. For example, the framed cloud features that possess low contrast and high noise of albedo should be  
21 removed. The cloud feature contrast can be characterized by the albedo amplitude for the largest scale  
22 variability within the matching frame [Rong et al., 2018].  
23  
24  
25  
26

27 The evolution of the small scale gravity wave structures enclosed in the matching frames is another  
28 interest of ours in the context of the CIPS cloud tracking. We will conduct the investigation beyond the  
29 case studies via obtaining the statistical results throughout the entire season and different years. Such small  
30 scale wave structures (i.e.,  $\sim 20$ -60 km) often vary by some degree but remain as semi-organized between  
31 two consecutive orbits. The CIP cloud tracking is an appropriate platform to examine whether they are the  
32 same wave structure transported by wind advection and how they have evolved between the two time  
33 stamps [Fogle and Haurwitz, 1966].  
34  
35  
36  
37  
38  
39  
40

## 41 **9. Conclusions**

42 We have thoroughly described the refined CIPS PMC wind tracking algorithm and assessed its first  
43 product relative to the NOGAPS winds and the HWM14 wind climatology. The sanity of the wind set is  
44 validated but more years of CIPS wind data are required to further assess whether CIPS cloud tracking is a  
45 reliable approach to create the long time series of the mesopause winds in the polar summer region.  
46  
47  
48  
49  
50

51 The CIPS zonal winds and meridional winds are westward and southward statistically, which  
52 conforms to the established wind climatology. The CIPS zonal wind speed is contained within 20 m/s  
53 throughout the season and is about 5-10 m/s smaller systematically than the NOGAPS or HWM14 winds in  
54 the corresponding LT range. The apparent cause of the smaller CIPS winds is likely the limitation on the  
55 allowed distance for frame movement even though there are occasions that cloud tracking result clearly  
56  
57  
58  
59  
60  
61  
62  
63  
64  
65

1 indicates smaller winds than in the NOGAPS at the coincidences. The CIPS meridional wind speed is  
2 within 10 m/s throughout the season which is very close to the NOGAPS result.  
3

4 For effective cloud tracking, the frame size for the cloud pattern matching shall be far greater than the  
5 pixel size and the movement of a full frame size shall be correspondent to the roughly maximum wind  
6 speed. We adopted three frame sizes which are 500 km as the default size used before, and 25% smaller  
7 and larger sizes respectively. Each given size refers to the length in the lon direction at the lowest lat of the  
8 frame. Choosing multiple frame sizes is to generate redundant wind detections to eventually achieve more  
9 robust wind set with better consistency and spatial coverage. In the CIPS PMC tracking algorithm the best  
10 match of a given cloud pattern is searched within one frame size in both lon and lat directions. Eventually  
11 achieving maximum Pearson correlation that exceeds 0.7 is used as the criterion of a successful match.  
12  
13  
14  
15  
16  
17  
18

19 The rationale of the frame size choice is explored via examining the CIPS PMC cloud feature  
20 memory, characterized by the correlation coefficient of the cloud feature within the same frame location  
21 between two adjacent orbits in the level-2 data. Better memory will lead to higher success rate of the  
22 pattern matching in the actual cloud wind tracking. The CIPS PMCs “remember” increasingly better of  
23 their history from 96 minutes ago when the frame size encloses larger area of cloud features, but we should  
24 keep in mind that choosing larger frame will practically reduce the number of independent cloud patterns  
25 which will eventually reduce the number of wind detections.  
26  
27  
28  
29  
30  
31  
32

33 Preliminary wind sets from the three frame sizes are first merged, and then screening/editing is  
34 applied within each regularly spaced grid-cell to eventually obtain a wind that is representative. In our first  
35 wind product the sampling grid-sizes used are  $1.5^{\circ}\text{lon}\times 1.5^{\circ}\text{lat}$  and  $4.5^{\circ}\text{lon}\times 4.5^{\circ}\text{lat}$  respectively, to test the  
36 self-consistency and the data quality. Within each grid-cell, winds are grouped into different clusters by  
37 similar directions ( $\pm 20^{\circ}$ ). If a wind does not pair up with any other wind in the grid-cell it is removed as a  
38 singularity. Different clusters are averaged eventually to obtain the mean wind in the grid-cell; if there is  
39 not any cluster then we select the wind with the minimum speed.  
40  
41  
42  
43  
44  
45

46 There is a definitive but low degree of deterministic consistency between the CIPS and NOGAPS  
47 winds at the coincidences. The agreements are widespread at all lons on CIPS orbits but the number of  
48 agreements (per orbit) is highly unbalanced between different orbits. Averaging over all orbits, the two  
49 wind sets can achieve about ~30% agreements if both the zonal and meridional winds are required to be in  
50 the consistent directions. The wind agreement and the ice distribution consistency have shown a  
51 quantitative causal link on the orbit-by-orbit basis, indicating that temperature is probably impacting both.  
52 The discrepancy could be due to three factors. First, the NAVDAS component is incorporated 6-hourly  
53 rather than 1-hourly and therefore the NOGAPS temperature is deviated from the true temperature. This  
54  
55  
56  
57  
58  
59  
60  
61  
62  
63  
64  
65

1 would affect the accuracy of both 0-D modeled ice and the geostrophic winds; second, CIPS winds contain  
2 ageostrophic components and are cascaded into smaller scales compared to the NOGAPS winds. Third,  
3 cloud tracking approach leads to false wind detections.  
4

5  
6 The CIPS zonal (westward) winds are decreased and reversed in early June and late August whereas  
7 in the core of the season they are stronger. This overall variation pattern is shared by both NOGAPS and  
8 HWM14 zonal winds, but the magnitudes and the detailed intra-seasonal variability differ between years or  
9 wind sets. For example, the NOGAPS zonal winds are persistently strong throughout the June, July, and  
10 August exhibiting a very mild intra-seasonal variability. It is especially noteworthy that the NOGAPS zonal  
11 winds averaged over the CIPS LT range (~13-22 hour) are ~8-10 m/s smaller than using all data in the 0-24  
12 hour LT times. The same LT dependence is echoed in the HWM14 zonal winds, which may partially  
13 interpret the systematically smaller CIPS zonal winds.  
14  
15

16  
17 The meridional (equatorward) winds do not follow any established intra-seasonal variation pattern  
18 but rather the variability is susceptible to the sampling lons/lats on a daily basis. The CIPS winds in 2009  
19 and 2007 exhibit drastically different intra-seasonal variation patterns. The NOGAPS winds sampled at the  
20 coincidences (with CIPS) in these two years also show the same inter-annual difference that is apparently  
21 caused by sampling on the ascending and descending nodes respectively. The HWM14 meridional wind  
22 climatology averaged in the CIPS LT range are persistently poleward, mainly due to the presence of  
23 distinctly dominant migrating tides. On the contrary, the NOGAPS meridional winds exhibit more complex  
24 tidal variability so that spatial averaging strongly suppresses the daily fluctuation. These results overall  
25 suggest that the meridional wind variability is more unpredictable and is more dependent on the sampling  
26 path, which is very different from the zonal winds.  
27  
28

29  
30 Regression analysis applied to the 10-day hourly time series of NOGAPS winds at 12 selected  
31 lons/lats (evenly distributed in the polar region) indicates that both tides and 2-10day variability modes  
32 contribute substantially in the wind variability but tidal variability is slightly dominant. Especially, when  
33 non-migrating tides are present, as is the case in the NOGAPS winds, aliasing can be significant when  
34 applying regression analysis to the asynoptic data such as the CIPS cloud tracking winds.  
35  
36

### 37 **Acknowledgement:**

38  
39 This work was supported by the NSF CEDAR award ID1651394 and NASA Small Explorer Program  
40 through contract NAS5-03132. We thank the NRL for providing the NOGAPS-ALPHA data. We are also  
41 extremely grateful to Dr. Douglas Drob for providing the Horizontal Wind Model (HWM14). We  
42 acknowledge all members of AIM science team, especially the CIPS science team and retrieval team, for  
43 their support on this project throughout the years. CIPS data can be accessed through website  
44  
45  
46  
47  
48  
49

1 <http://lasp.colorado.edu/aim/download-data-pmc.php>. We are also grateful to Dr. Dong L. Wu from NASA  
2 and Dr. Jie Gong from USRA for providing the initiatives in the early stage of this research project.  
3

#### 4 **References:**

5  
6  
7 Bailey, S. M., C. E. Randall, J. D. Lumpy, M. E. Hervig, G. E. Thomas, and J. M. Russell (2009), Phase  
8 functions of polar mesospheric cloud ice as observed by the CIPS instrument on the AIM satellite, *J.*  
9 *Atmos. Sol. Terr. Phys.*, 71, 373–380, doi:10.1016/j.jastp.2008.09.039.  
10

11  
12  
13 Baumgarten, G., F.-J. Lübken, and K. H. Fricke (2002), First observation of one noctilucent cloud by a  
14 twin lidar in two different directions, *Ann. Geophys.*, 20(11), 1863–1868.  
15

16  
17 Berger, U., and U. von Zahn (2007), Three-dimensional modeling of the trajectories of visible noctilucent  
18 cloud particles: An indication of particle nucleation well below the mesopause, *J. Geophys. Res.*, 112,  
19 D16204, doi:10.1029/2006JD008106.  
20

21  
22  
23 Dalin, P., et al. (2013), Optical studies of rocket exhaust trails and artificial noctilucent clouds produced by  
24 Soyuz rocket launches, *J. Geophys. Res. Atmos.*, 118, 7850–7863, doi:10.1002/jgrd.50549.  
25

26  
27 Dowdy, A. J., R. A. Vincent, M. Tsutsumi, K. Igarashi, Y. Murayama, W. Singer, and D. J. Murphy  
28 (2007), Polar mesosphere and lower thermosphere dynamics: 1. Mean wind and gravity wave  
29 climatologies, *J. Geophys. Res.*, 112, D17104, doi:10.1029/2006JD008126.  
30

31  
32  
33 Drob, D. P., et al. (2008), An empirical model of the Earth's horizontal wind fields: HWM07, *J. Geophys.*  
34 *Res.*, 113, A12304, doi:10.1029/2008JA013668.  
35

36  
37 Drob, D. P., et al. (2015), An update to the Horizontal Wind Model (HWM): The quiet time thermosphere,  
38 *Earth and Space Science*, 2, 301–319, doi:10.1002/2014EA000089.  
39

40  
41 Eckermann, S. D., K. W. Hoppel, L. Coy, J. P. McCormack, D. E. Siskind, K. Nielsen, A. Kochenash, M.  
42 H. Stevens, C. R. Englert, and M. Hervig (2009), High-altitude data assimilation system experiments for  
43 the northern summer mesosphere season of 2007, *J. Atmos. Sol. Terr. Phys.*, 71, 531–551.  
44

45  
46  
47 Foerster, W., and O. Jesse (1892), Invitation to observe the luminous night clouds, *Nature*, 46, 589–590,  
48 doi:10.1038/046589a0.  
49

50  
51 Fogle, B., and B. Haurwitz (1966), Noctilucent clouds, *Space Sci. Rev.*, 6(3), 279–340.  
52

53  
54 Hays, P. B., V. J. Abruë, M. E. Dobbs, D. A. Gell, H. J. Grassl, and W. R. Skinner (1993), The high-  
55 resolution doppler imager on the Upper Atmosphere Research Satellite, *J. Geophys. Res.*, 98, 10,713 –  
56 10,723, doi:10.1029/93JD00409.  
57  
58  
59  
60  
61  
62  
63  
64  
65

1 Hervig, M. E., M. H. Stevens, L. L. Gordley, L. E. Deaver, J. M. Russell, and S. Bailey (2009),  
2 Relationships between PMCs, temperature and water vapor from SOFIE observations, *J. Geophys. Res.*,  
3 114, D20203, doi:10.1029/2009JD012302.  
4

5  
6 Garcia, R. R., and S. Solomon (1985), The effect of breaking gravity waves on the dynamics and chemical  
7 composition of the mesosphere and lower thermosphere, *J. Geophys. Res.*, 90(D2), 3850–3868,  
8 doi:10.1029/JD090iD02p03850.  
9

10  
11 Garcia, R. R. (1989), Dynamics Radiation and Photochemistry in the Mesosphere: Implication for the  
12 Formation of the Noctilucent Clouds, *J. Geophys. Res.*, 94, D12, 14,605-14,615.  
13

14  
15 Garcia, R. R., R. Lieberman, J. M. Russell III, and M. G. Mlynczak (2005), Large-scale waves in the  
16 mesosphere and lower thermosphere observed by SABER, *J. Atmos. Sci.*, 62, 4384-4399.  
17

18  
19 Horváth, Á., and R. Davies, 2001: Feasibility and error analysis of cloud motion wind extraction from near-  
20 simultaneous multiangle MISR measurements. *J. Atmos. Oceanic Technol.*, 18, 591–608,  
21 doi:10.1175/1520-0426(2001)018,0591:FAEAO.2.0.CO;2.  
22

23  
24 Hervig, M. E., M. H. Stevens, L. L. Gordley, L. E. Deaver, J. M. Russell III, and S. M. Bailey (2009),  
25 Relationships between PMCs, temperature and water vapor from SOFIE observations, *J. Geophys. Res.*,  
26 114, D20203, doi:10.1029/2009JD012302.  
27

28  
29 Hoffmann, P., M. Rapp, W. Singer, and D. Keuer (2011), Trends of mesospheric gravity waves at northern  
30 middle latitudes during summer, *J. Geophys. Res.*, 116, D00P08, doi:10.1029/2011JD015717  
31

32  
33 Jensen, E., and G. E. Thomas (1988), A growth-sedimentation model of polar mesospheric clouds:  
34 Comparison with SME measurements, *J. Geophys. Res.*, 93, 2461–2473, doi:10.1029/JD093iD03p02461.  
35

36  
37 Latteck, R., W. Singer, M. Rapp, B. Vandeppeer, T. Renkwitz, M. Zecha, and G. Stober (2012), MAARSY:  
38 The new MST radar on Andøya-System description and first results, *RADIO SCIENCE*, 47, RS1006,  
39 doi:10.1029/2011RS004775.  
40

41  
42 Lübken, F.-J. and A. Müllemann (2004), Temperatures and horizontal winds in the Antarctic summer  
43 mesosphere, *J. Geophys. Res.*, 109, D24112, doi:10.1029/2004JD005133.  
44

45  
46 Lukianova, R., A. Kozlovsky, M. Lester (2018), Climatology and inter-annual variability of the polar  
47 mesospheric winds inferred from meteor radar observations over Sodankylä (67N, 26E) during solar cycle  
48 24, *JASTP*, 171 (2018) 241–249.  
49  
50  
51  
52  
53  
54  
55  
56  
57  
58  
59  
60  
61  
62  
63  
64  
65

1 Lumpe, J. D., et al. (2013), Retrieval of polar mesospheric cloud properties from CIPS: Algorithm  
2 description, error analysis and cloud detection sensitivity, *J. Atmos. Sol. Terr. Phys.*, 104, 167–196,  
3 doi:10.1016/j.jastp.2013.06.007.  
4  
5  
6 McClintock, W. E., D. W. Rusch, G. E. Thomas, A. W. Merkel, M. R. Lankton, V. A. Drake, S. M. Bailey,  
7 and J. M. Russell III (2009), The cloud imaging and particle size experiment on the Aeronomy of Ice in the  
8 Mesosphere mission: Instrument concept, design, calibration, and on-orbit performance, *J. Atmos. Sol.*  
9 *Terr. Phys.*, 71, 340–355, doi:10.1016/j.jastp.2008.10.011.  
10  
11  
12 McCormack, J. P., L. Coy, and K. W. Hoppel (2009), Evolution of the quasi 2-day wave during January  
13 2006, *J. Geophys. Res.*, 114, D20115, doi:10.1029/2009JD012239.  
14  
15  
16 McCormack, J. P., L. Coy, and W. Singer (2014), Intraseasonal and interannual variability of the quasi  
17 2day wave in the Northern Hemisphere summer mesosphere, *J. Geophys. Res. Atmos.*, 119, 2928–2946,  
18 doi:10.1002/2013JD020199.  
19  
20  
21  
22 Merkel, W. A., D. W. Rusch, S. E. Palo, J. M. Russell III, and S. M. Bailey (2009), Mesospheric planetary  
23 wave activity inferred from AIM-CIPS and TIMED-SABER for the northern summer 2007 PMC season, *J.*  
24 *Atmos. Sol. Terr. Phys.*, doi:10.1016/j.jastp.2006.05.01.  
25  
26  
27  
28  
29  
30 Menzel, W. P. (2001), Cloud tracking with satellite imagery: From the pioneering work of Ted Fujita to the  
31 present, *Bull. Am. Meteorol. Soc.*, 82, 33–47, doi:10.1175/1520-0477(2001)082<0033:CTWSIF>2.3.CO;2.  
32  
33  
34  
35 Mertens, C. J., et al. (2004), SABER observations of mesospheric temperatures and comparisons with  
36 falling sphere measurements taken during the 2002 summer MaCWAVE campaign. *Geophysical Research*  
37 *Letters* 31, L03105.  
38  
39  
40  
41 Mueller, K., C. Moroney, V. Jovanovic, M. J. Garay, J-P Muller, L D. Girolamo, and R. Davies, MISR  
42 Level 2 Cloud Product Algorithm Theoretical Basis (2013), JPL D-73327.  
43  
44  
45 MUELLER, K. J., D. L. WU, Á. HORVÁTH, V. M. JOVANOVIĆ, J-P MULLER, L. DI GIROLAMO, M.  
46 J. GARAY, D. J. DINER, C. M. MORONEY, and S. WANZONG (2017), Assessment of MISR Cloud  
47 Motion Vectors (CMVs) Relative to GOES and MODIS Atmospheric Motion Vectors (AMVs), *J. APP.*  
48 *METEO. AND CLIM.*, DOI: 10.1175/JAMC-D-16-0112.1.  
49  
50  
51  
52  
53 Murayama, Y., K. Igarashi, D. Rice, B. Watkins, R. Collins, K. Mizutani, Y. Saito, and S. Kainuma (2000),  
54 Medium frequency radars in Japan and Alaska, for upper atmosphere observations, *IEICE Trans. Fundam.*  
55 *Electron. Commun. Comput. Sci.*, E83-B, 1996– 2003.  
56  
57  
58  
59 Portnyagin, Y., et al. (2004a), Monthly mean climatology of the prevailing winds and tides in the Arctic  
60 mesosphere/lower thermosphere, *Ann. Geophys.*, 22, 3395–3410, doi:10.5194/angeo-22-3395-2004.  
61  
62  
63  
64  
65

1 Portnyagin, Y., et al. (2004b), Mesosphere/lower thermosphere prevailing wind model, *Adv. Space Res.*,  
2 34, 1755–1762.  
3  
4 Rapp, M., F.-J. Lübken, A. Müllemann, G. E. Thomas, and E. J. Jensen (2002), Small scale temperature  
5 variations in the vicinity of NLC: Experimental and model results, *J. Geophys. Res.*, 107(D19), 4392,  
6 doi:10.1029/2001JD001241.  
7  
8 Renkwitz, T., M. Tsutsumi, F. I. Laskar, J. L. Chau, and R. Latteck (2018), On the role of anisotropic  
9 MF/HF scattering in mesospheric wind estimation, *Earth, Planets and Space* 70:158  
10 <https://doi.org/10.1186/s40623-018-0927-0>.  
11  
12 Rong, P. P., J. M. Russell III, C. E. Randall, S. M. Bailey, and A. Lambert (2014), Northern PMC  
13 brightness zonal variability and its correlation with temperature and water vapor, *J. Geophys. Res. Atmos.*,  
14 119, 2390–2408, doi:10.1002/2013JD020513.  
15  
16 Rong, P. P., J. Yue, J. M. Russell III, J. D. Lumpe, J. Gong, D. L. Wu, and C. E. Randall (2015), Horizontal  
17 winds derived from the polar mesospheric cloud images as observed by the CIPS instrument on the AIM  
18 satellite, *J. Geophys. Res. Atmos.*, 120, 5564–5584, doi:10.1002/2014JD022813.  
19  
20 Rong, P. P., J. Yue, J. M. Russell III, D. E. Siskind, and C. E. Randall (2018), Universal power law of the  
21 gravity wave manifestation in the AIM CIPS polar mesospheric cloud images, *Atmos. Chem. Phys.*, 18,  
22 883–899, <https://doi.org/10.5194/acp-18-883-2018>.  
23  
24 Russell, J. M., III, et al. (2009), Aeronomy of Ice in the Mesosphere (AIM) mission: Overview and early  
25 science results, *J. Atmos. Sol. Terr. Phys.*, 71(3–4), 289–299, doi:10.1016/j.jastp.2008.08.011.  
26  
27 Russell, J. M., III, P. Rong, S. M. Bailey, M. E. Hervig, and S. V. Petelina (2010), Relationship between  
28 the summer mesopause and polar mesospheric cloud heights, *J. Geophys. Res.*, 115, D16209,  
29 doi:10.1029/2010JD013852.  
30  
31 Salby, M. L., (1982), Sampling theory for asynoptic satellite observations. Part II: Fast Fourier synoptic  
32 mapping. *J. Atmos. Sci.*, **39**, 2601–2614.  
33  
34 Schmidlin, et al. (1985), Rocket techniques used to measure the neutral atmosphere, International Council  
35 of Scientific Unions Middle Atmosphere Program: Handbook for MAP, vol. 19, edited by R. A. Goldberg,  
36 pp. 1 – 28, Inst. of Appl. Geophys., Moscow.  
37  
38 Schwartz, M. J., et al. (2008), Validation of the aura microwave limb sounder temperature and geopotential  
39 height measurements, *J. Geophys. Res.* 113, D15S11.  
40  
41  
42  
43  
44  
45  
46  
47  
48  
49  
50  
51  
52  
53  
54  
55  
56  
57  
58  
59  
60  
61  
62  
63  
64  
65

1 Siskind, D. E., D. P. Drob, J. T. Emmert, M. H. Stevens, P. E. Sheese, E. J. Llewellyn, M. E. Hervig, R.  
2 Niciejewski, and A. J. Kochenash (2012), Linkages between the cold summer mesopause and  
3 thermospheric zonal mean circulation, *Geophys. Res. Lett.*, 39, L01804, doi:10.1029/2011GL050196.

4  
5  
6 Stevens, M. H., et al. (2010), Tidally induced variations of polar mesospheric cloud altitudes and ice water  
7 content using a data assimilation system, *J. Geophys. Res.*, 115, D18209, doi:10.1029/2009JD013225.

8  
9  
10 Stevens, M. H., R. S. Lieberman, D. E. Siskind, J. P. McCormack, M. E. Hervig, and C. R. Englert (2017),  
11 Periodicities of polar mesospheric clouds inferred from a meteorological analysis and forecast system, *J.*  
12 *Geophys. Res. Atmos.*, 122, doi:10.1002/2016JD025349.

13  
14  
15  
16 Stober, G., R. Latteck, M. Rapp, W. Singer, and M. Zecha (2012), MAARSY – the new MST radar on  
17 Andøya: first results of spaced antenna and Doppler measurements of atmospheric winds in the troposphere  
18 and mesosphere using a partial array, *Adv. Radio Sci.*, 10, 291–298, [www.adv-radio-sci.net/10/291/2012/](http://www.adv-radio-sci.net/10/291/2012/)  
19 doi:10.5194/ars-10-291-2012.

20  
21  
22  
23 TALAAT, E. R. and R. S. LIEBERMAN (1999), Nonmigrating Diurnal Tides in Mesospheric and Lower-  
24 Thermospheric Winds and Temperatures, *J. Atmos. Sci.*, 56(24).

25  
26  
27  
28 Wu., D. L., D. Halpern, K. J. Mueller, E. Rodriguez, M. J. Kavaya, U. N. Singh, S. Tucker, G. D. Emmitt,  
29 C. S. Ruf, and Á. Horváth (2015), NASA Global Wind Measurements and Technology Development,  
30 CGMS-43 NASA-WP-05, v1, 18 May 2015.

### 31 32 33 34 **Figure captions:**

35  
36  
37 Figure 1: (a) The grid system used for the CIPS wind tracking pattern matching. The grid length is 5 km in  
38 both longitudinal and latitudinal directions but here for demonstration purpose we have shown as 50 km  
39 grid length. (b) Daily mean number of wind detections based on different correlation coefficient thresholds.  
40 The dashed lines are standard deviation for July mean detection number over different correlation  
41 coefficient thresholds (solid lines).

42  
43  
44 Figure 2: The histograms of the correlation coefficients of the same-location cloud features between two  
45 orbits (i.e., 96 minutes apart) within the given frame. The different panels are different frame sizes. The  
46 DOYs 191, 193, and 195 in 2007 are used to build these statistical sets. The wind registration on the upper  
47 horizontal axis is based on the assumption that a wave-1 sinusoidal cloud pattern is displaced by wind  
48 advection solely.

49  
50  
51  
52 Figure 3: Demonstration of the three frame sizes (a-c) for the pattern matching wind determination. The  
53 upper and lower panels are two consecutive orbits that are 96 minutes apart. Red is for original frame  
54 position and green encloses the cloud pattern that is the best match from the next orbit. The orange color in  
55 the lower panels marks the position of the first orbit. In (c) the thin dotted red lines indicate possible  
56 straight wave ridges in this particular case.

57  
58  
59  
60 Figure 4: The cloud features enclosed in the red (upper) and green (lower) frames in Figure 3 respectively.

1 Figure 5: (a) Black: histogram of correlation coefficients (over any given CIPS orbit) between the  
2 NOGAPS 0-D ice and CIPS measured ice at the coincidences throughout the summer in 2009. Red: same  
3 as the black except for correlation coefficients between the NOGAPS 0-D ice and the temperature used to  
4 generate the 0-D ice. (b) Intra-seasonal variations of the daily largest to median correlation coefficients  
5 between NOGAPS 0-D ice and CIPS measured ice.  
6

7  
8 Figure 6: The demonstration of the CIPS cloud tracking winds overlapped on the CIPS albedo orbital strips.  
9 The orange vectors are identical for the three panels while in (b) and (c) the color-filled fields are CIPS  
10 albedo over the two adjacent orbits. The legends of zonal and meridional winds (U and V) of 50 m/s exhibit  
11 different lengths due to the display ratio.  
12  
13

14  
15 Figure 7: (a-b) The CIPS and NOGAPS winds with consistent (thick orange) and inconsistent (thin black)  
16 directions in both zonal (U) and meridional winds (V) at coincidences on DOY 185 2009 on the CIPS orbit  
17 close to UT hour 21. (c) NOGAPS winds (black arrows) and geopotential height field (color-filled) on the  
18 NOGAPS grid points in the same latitude range (72°-86°N).  
19  
20

21  
22 Figure 8: Demonstration of CIPS (a) and NOGAPS (b) directional agreements (in both U and V) on all the  
23 orbits for DOY 185 2009, with the rainbow colors (black to red) representing smaller to larger UT hours.  
24 Wind vector legend is the same as in Figures 6 and 7.  
25

26  
27 Figure 9: The fraction of agreements, i.e., characterized by the slope in the legend, between the CIPS and  
28 NOGAPS winds at the coincidences over the entire season. The (a) and (d) are for U agreements only, (b)  
29 and (e) are for V agreements only, and (c) and (f) are for cases of both U and V being in consistent  
30 directions between the two wind sets. Upper and lower panels are for cases with and without wind  
31 thresholds respectively. The wind thresholds are elaborated in Figure 2.  
32  
33

34  
35 Figure 10: (a)-(b) The daily time series of the ratios between the largest, 2<sup>nd</sup> largest, or 3<sup>rd</sup> largest agreement  
36 numbers and the median wind agreement number per orbit. This indicates that wind agreement numbers  
37 between CIPS and NOGAPS are highly unbalanced among the CIPS orbits. The (a) and (b) used different  
38 criteria to determine directional agreement between the two wind sets as indicated in the legend. (c) The  
39 relationship between the ice agreement and wind agreement per orbit. The ice agreement is characterized  
40 by the spatial correlation coefficient of the modeled and measured ice, and the wind agreement refers to the  
41 directional agreement as defined above.  
42  
43  
44

45  
46 Figure 11: (a) The CIPS local time coverage demonstrated over three days in the two selected years. (b)  
47 The daily mean latitude time series of the CIPS wind detections. The averaged standard deviation (STD)  
48 throughout the season is given in the legend. The smooth curves are 2<sup>nd</sup> order polynomial fits.  
49

50  
51 Figure 12: The daily mean U series in the CIPS winds (a-d) and the counterpart in NOGAPS winds  
52 sampled at the CIPS coincidences (e-f). The number of detections throughout the season and the seasonal  
53 mean of daily standard error of mean (SEM) are indicated in the legend. The (a) and (c) or (b) and (d) are  
54 pairs of with and without wind thresholds in CIPS. The CIPS wind subsets are about 29% of the total wind  
55 detections, as marked. The “corr” numbers in the legends in the middle panels are the correlation  
56 coefficients between (a) and (c), (b) and (d) respectively. The “corr” number in the legend in (f) is the  
57 correlation coefficient between (e) and (f). All fitting curves are 2<sup>nd</sup> order polynomials.  
58  
59  
60  
61  
62  
63  
64  
65

1 Figure 13: Same as Figure 12 except for the meridional wind (V).

2  
3 Figure 14: (a)-(b) The NOGAPS wind daily mean series (U and V) using all data in 70°-86°N (black  
4 curves) and using the data exclusively in the CIPS local time range (12-22<sup>th</sup> hour, red fills). The thick  
5 smooth curves are 2<sup>nd</sup> order polynomial fits. Note that in (b) the smooth curves used the right vertical axis  
6 for scale for better presentation.

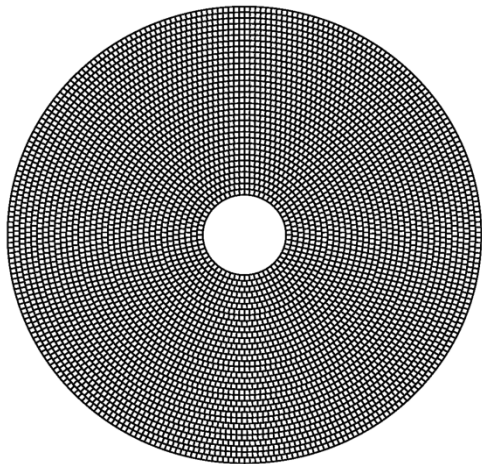
7  
8  
9 Figure 15: Same as Figure 14 except using the Horizontal Wind Model 2014 (HWM14) output.

10  
11 Figure 16: Demonstration of the decomposed NOGAPS U and V time series at one grid point (lon=0,  
12 lat=80°N) on the 0.00436 hPa surface into tides with periods of one-day to 1/4<sup>th</sup> day combined (in red) and  
13 low frequency fluctuation with periods of 2-10 days combined (in green).

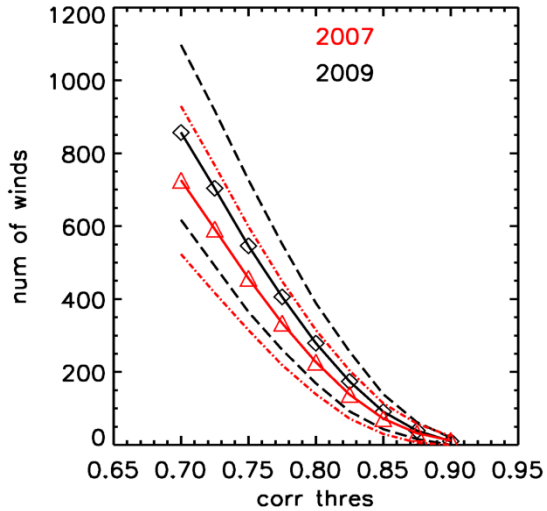
14  
15  
16 Figure 17: (a-b) are the 10-day smoothed intra-seasonal time series of the mean diurnal and semi-diurnal  
17 amplitudes respectively. (c-d) are for the 2-day and 5-day fluctuation modes respectively. In each of the 12  
18 individual analyses, linear regression is applied to a 10-day hourly time series as demonstrated in Figure  
19 16. The vertical bars are the STDs of the 12 spatial locations combining the latitudes of 75°N, 80°N, and  
20 85°N, and longitudes of 0°E, 90°E, 180°E, and 180°W.

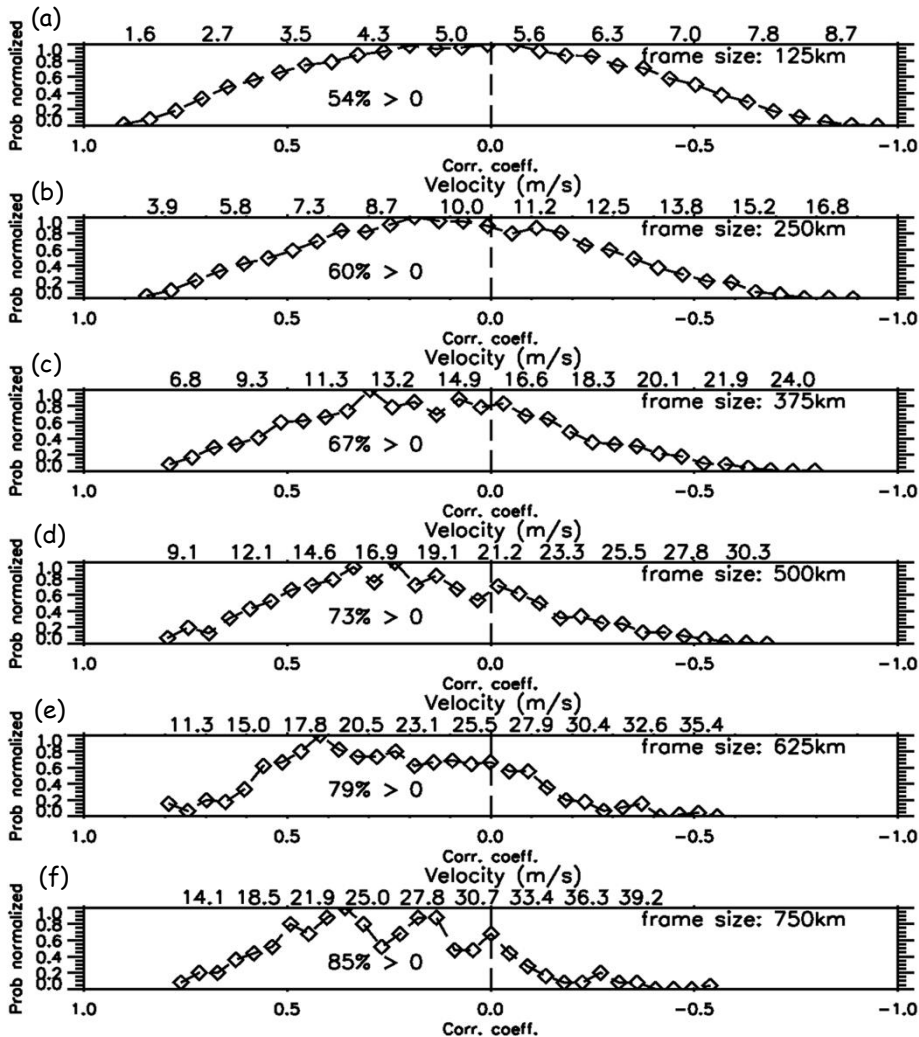
21  
22  
23  
24 Figure 18: (a-b) Daily time series of the CIPS cloud tracking winds (U and V) in 2009, screened and edited  
25 within grids 1.5°×1.5° (black) and 4.5°×4.5° (red), respectively. The error is the averaged SEM throughout  
26 the season and the two sampling grid sizes. Other numbers in the legends have the same meaning as in  
27 Figure 12.  
28  
29

(a)

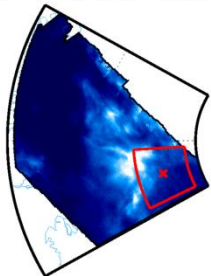


(b)

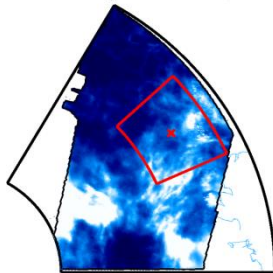




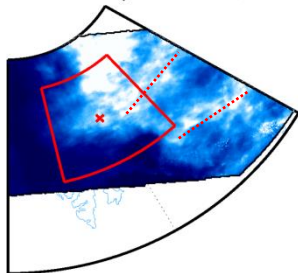
(a)  
DOY=185, time=21.2 hr



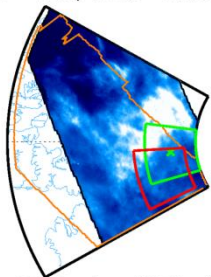
(b)  
DOY=185, time=13.1 hr



(c)  
DOY=185, time=17.9 hr

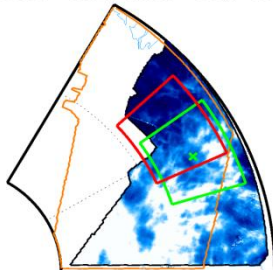


DOY=185, time=22.8 hr



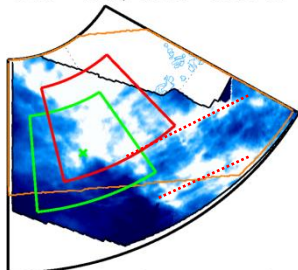
$u = -21.39\text{m/s}$  /  $sv = 11.57\text{m/s}$

DOY=185, time=14.7 hr

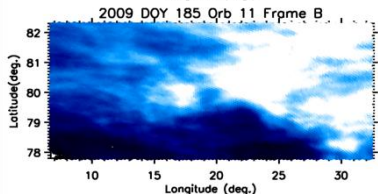
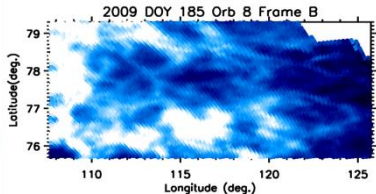
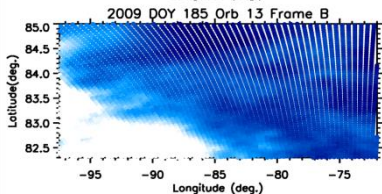
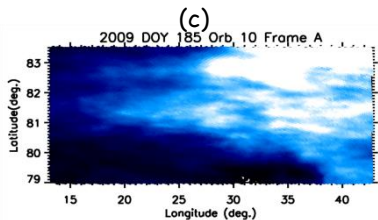
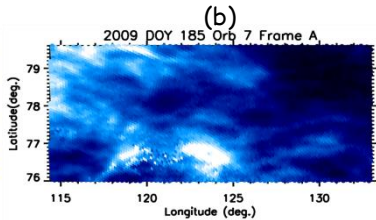
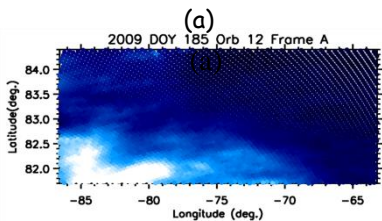


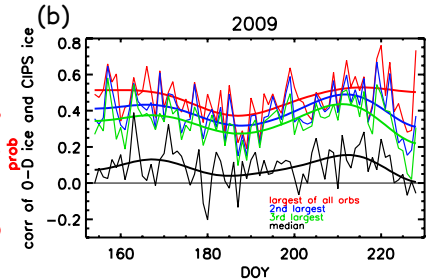
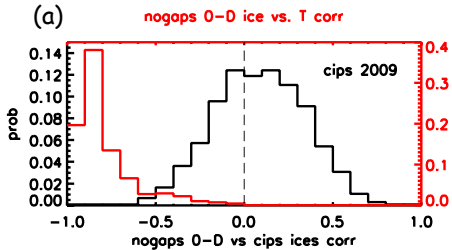
$u = -28.63\text{m/s}$  /  $sv = -5.76\text{m/s}$

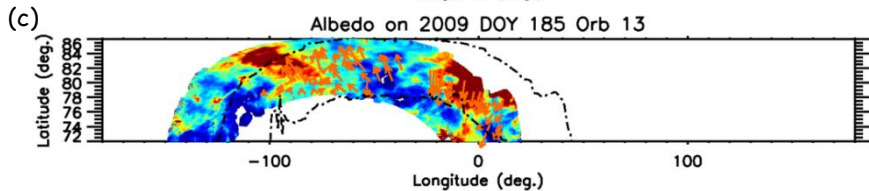
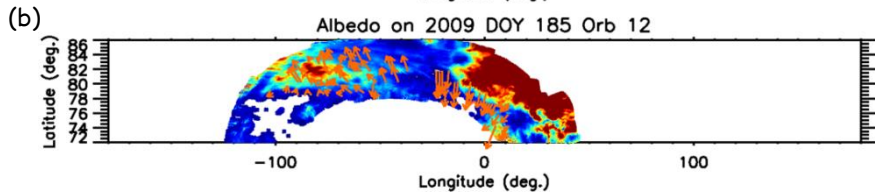
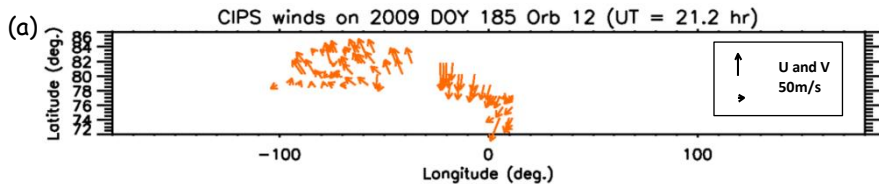
DOY=185, time=19.5 hr

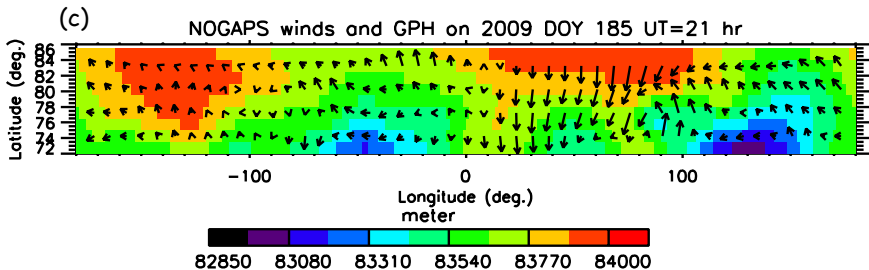
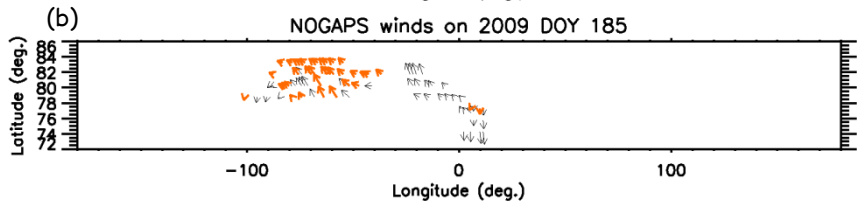
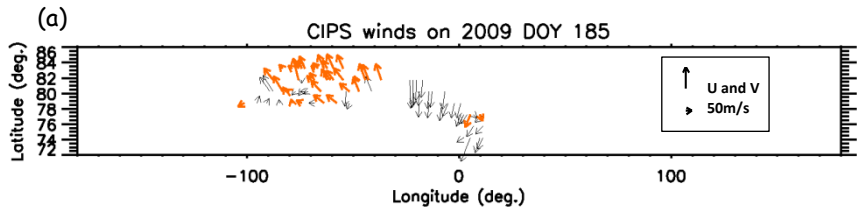


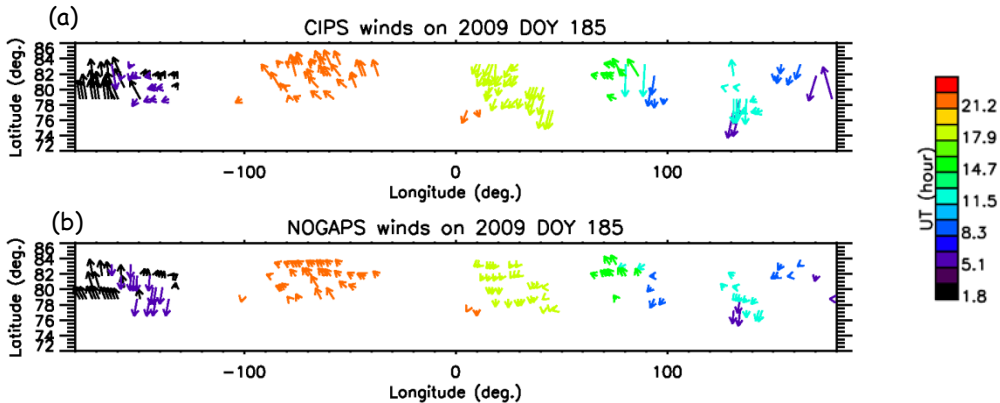
$u = -25.38\text{m/s}$  /  $sv = -23.06\text{m/s}$

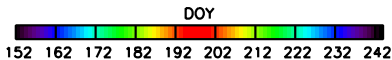
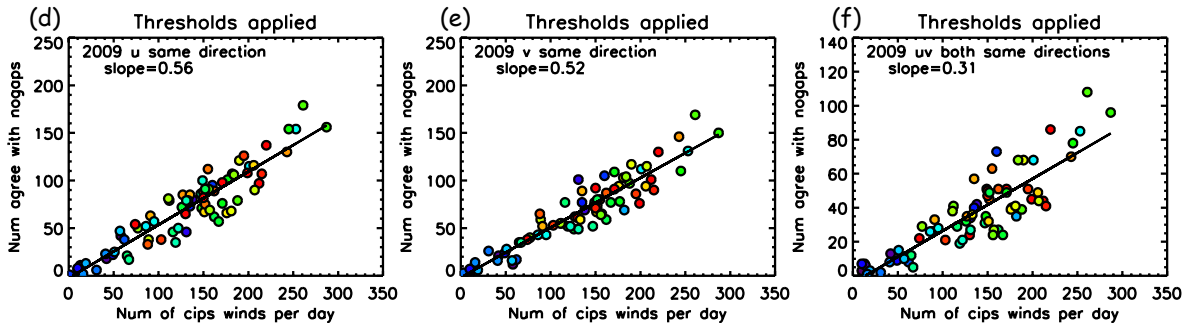
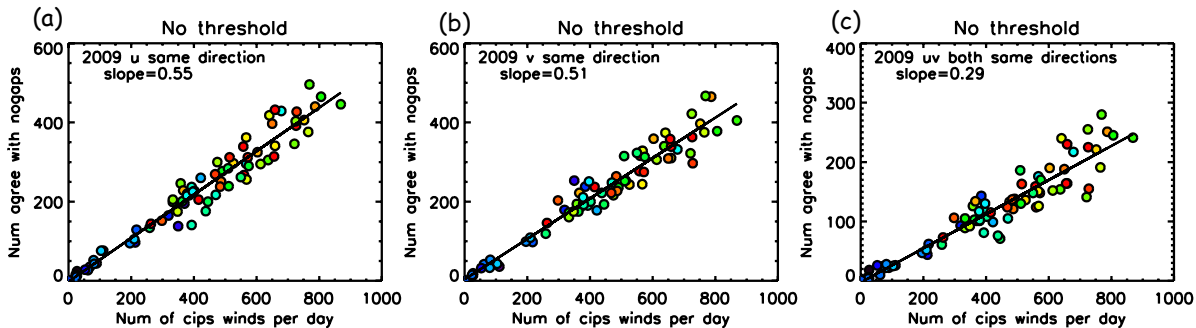


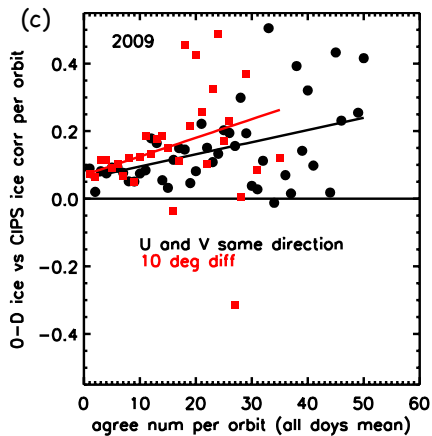
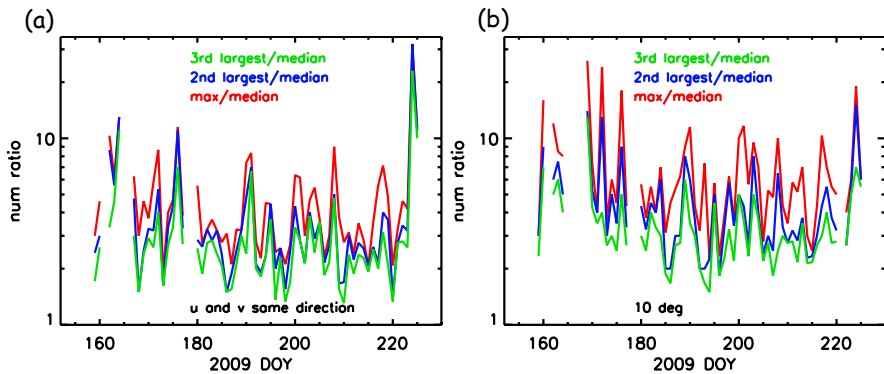


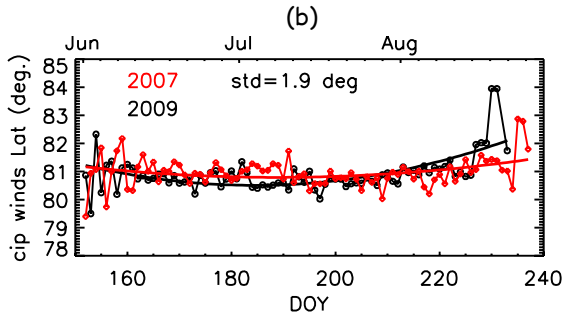
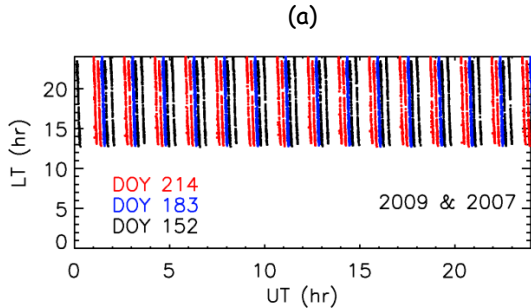


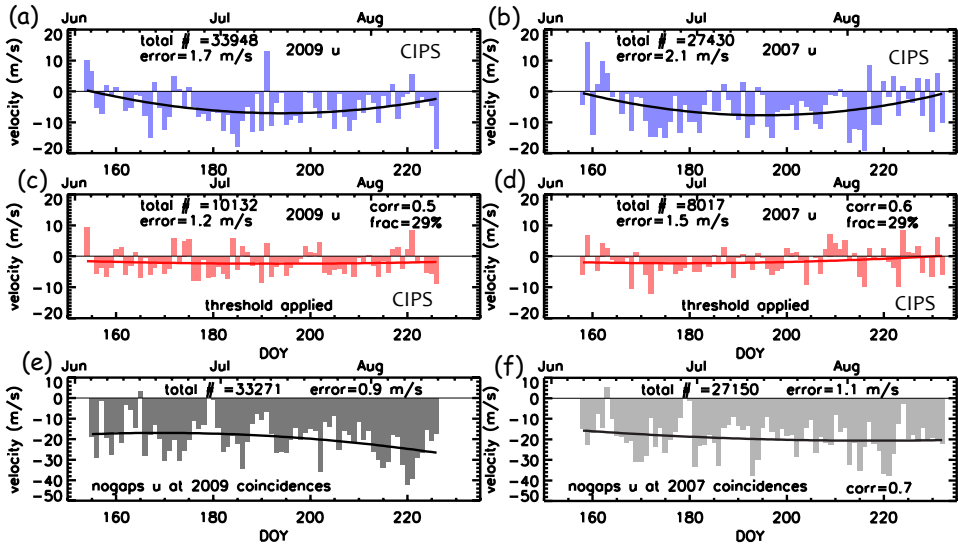


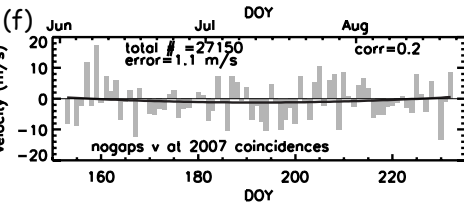
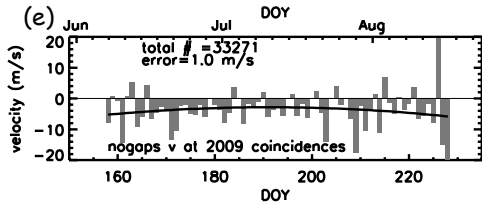
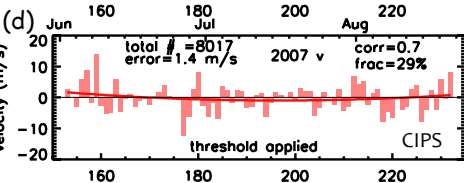
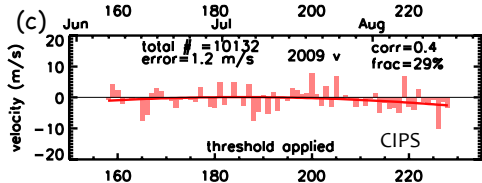
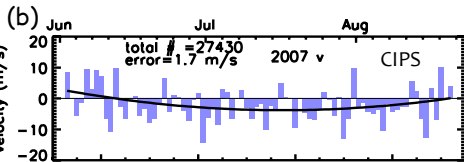
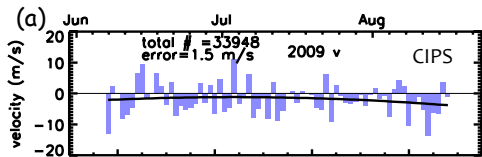


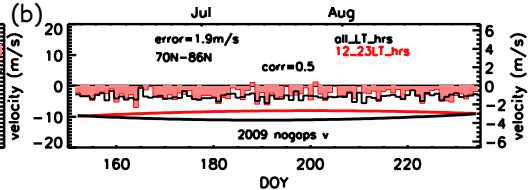
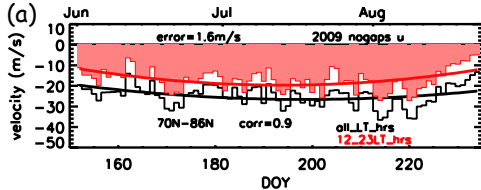






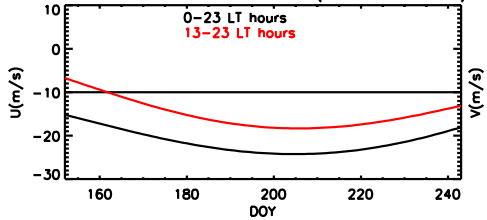






(a)

HWM14 zonal winds at 83km (70N–86N mean)



(b)

HWM14 meridional winds at 83km (70N–86N mean)

